Supplementary Information (SI) for Journal of Materials Chemistry A.
This journal is © The Royal Society of Chemistry 2026

Supporting Information

Engineering Intermolecular Charge Transfer in Covalent Organic Frameworks for Photocatalytic Hydrogen Peroxide Generation

Avanti Chakraborty,[a] Uttam Pal,[b,c] Sonali Priyadarshini Swain,[a] Sudipa Mondal,[a] Akhtar Alam,[a] Tanusri Saha-Dasgupta[b,c] and Pradip Pachfule*[a,c]*

[a]Department of Chemical and Biological Sciences, S. N. Bose National Centre for Basic Sciences, Kolkata – 700106, India**. E-mail:** ps.pachfule@bose.res.in.

[b]Department of Condensed Matter and Materials Physics, S. N. Bose National Centre for Basic Sciences, Kolkata – 700106, India. E-mail: tanusri@bose.res.in.

[c]Technical Research Centre, S. N. Bose National Centre for Basic Sciences, Kolkata – 700106, India.

Table of Contents

Section S1. Materials and Methods:

Organic precursors such as 4,4′,4′’-(1,3,5-Triazine-2,4,6-triyl) trianiline (TTT) and 4',4''',4''''-(1,3,5-triazine-2,4,6-triyl)tris(([1,1'-biphenyl]-4-amine)) (Extended TTT) have been synthesized using the reported procedures.[1-2] Organic precursors such as Thieno[3,2-b]thiophene-2,5-dicarbaldehyde (DTDA), 1,3,5-Tris(4-aminophenyl) benzene (TAPB), 4,4',4''-Triaminotriphenylamine (TAA), anhydrous 1,4-dioxane (99.9%), mesitylene (99 %), acetic acid (98 %), methanol (99 %),1,2-dichlorobenzene (*o*-DCB, AR grade, 99%), tetrahydrofuran (99 %), acetone (>99 %), HPLC water, *tert*-butanol (AR grade), *p*-benzoquinone (99%), ethanol (ACS grade, 99%), silver nitrate (99%), titanium (IV) oxsulfate-sulfuric acid solution (27-31% H_2SO_4) and peroxide test kits were purchased from Sigma-Aldrich and BLD Pharm. All reagents and solvents of analytical reagents were used without further purification.

Instrumentation

Powder X-ray powder diffraction (PXRD): PXRD patterns were performed on a PANalytical X-PERT PRO X-ray diffractometer with Cu Kα radiation (λ = 0.154 nm) at 2θ = 2-60°.

Nitrogen adsorption-desorption analysis: Nitrogen sorption isotherms were performed at 77K to evaluate the porosity property of as-synthesized COFs using a 3flex Micromeritics analyzer. Each sample (60-100 mg) was degassed at 120 °C under the flow of nitrogen for 8 hours prior to measurement. The specific surface area of the samples was estimated using the Brunauer-Emmett-Teller (BET) method.

Fourier transform infrared (FT-IR): The chemical functionalities and formation of desired linkages were confirmed by FT-IR spectra recorded by VERTEX 70v equipped with an ATR cell.

Solid-state ^{13}C CP/MAS NMR: The solid-state ^{13}C cross-polarization magic angle spinning (^{13}C CP/MAS NMR) NMR spectrum of the COF samples was recorded on a Bruker DPX-300 NMR spectrometer equipped with a spinning rate of 10 kHz.

UV-Vis diffuse reflectance spectra (UV-Vis DRS): UV-Vis spectra of the as-synthesized COFs were recorded by a UV-visible spectrophotometer (UV-2600, Shimadzu Corp., Japan) with an integrating sphere attachment and $BaSO_4$ reference.

FESEM Analysis: The morphology of the as-synthesized COFs was observed by field emission scanning electron microscopy using FESEM: FEI QUANTA FEG 250. The accelerating voltage was maintained at 200 kV. A drop of sample solution was drop-cast on a silicon wafer and dried properly before the analysis.

TEM Analysis: The morphology of the as-synthesized COFs was characterized by transmission electron microscopy (TEM: FEI TECNAI G2 F20-ST) using an accelerating voltage of 200 kV. The COF powder was dispersed in ethanol solution and drop-cast on the carbon-coated copper grid, respectively. Then, all the grids containing the samples were dried under an infrared lamp.

TGA Analysis: Thermogravimetric analysis (TGA) was performed with PerkinElmer TG-GC/MS (TGA 4000 coupled to the Clarus SQ8 GC/MS). The weight loss of the samples was recorded in the temperature range of 30−800 °C with a rate of 10°C/min under the flow of nitrogen (20 mL/min).

Photoluminescence (PL) measurements: PL measurements were carried out on a Fluorolog (HORIBA, JOBIN, YVON) instrument.

Electron paramagnetic resonance (EPR) measurements: Spin trapping EPR tests were recorded using a JEOL model FA200 X-band (9.5 GHz). 5,5-Dimethyl-1-pyrroline N-oxide (DMPO) was used as a spin-trapping reagent to detect $^{\bullet}OH$ or $O_2^{\bullet-}$. In particular, the catalysts (2 mg) were dispersed into water or a MeOH/water mixture (9/1 v/v, 500 μL) containing DMPO (0.1 mmol), in a Pyrex glass tube. A Xe lamp (λ = 467 nm) was used as the light source. The dispersion was purged with or O_2 gas for 5-10 min before light irradiation. The DMPO spin trapping EPR spectra were collected at 77 K and 298 K.

Gas Chromatography- Mass Spectrometry (GC-MS)

GC-MS was performed on a Thermo Scientific ISQ QD Mass Spectrometer attached to Thermo Scientific TRACE 1300 gas chromatograph using an HP-5 ms capillary column (30 m * 0.25mm * 0.25μm, J & W Scientific) with helium as the carrier gas. GC-MS method: oven temperature program, 18 min; initial temperature, 60 °C, hold for 2.00 min; ramp-1, 15 °C min-1 to 180°C, hold for 1 min; ramp-2, 20 °C min-1 to 280°C, hold for 1 min; injector temperature, 220°C; detector temperature, 280 °C.

Apparent quantum yield determination

The apparent quantum yield (AQY) of the COF-based photocatalysts was evaluated under the irradiation of Xe lamp (40 W) with 390, 440, 467 and 510 nm for 2 hours. The AQY was determined according to the following equation:

$$\text{AQY} = \frac{[\text{Number of formed } H_2O_2 \text{ molecules}] \times 2}{\text{Number of incident photons}} \times 100\% \quad (1)$$

$$\text{AQY} = \frac{(M_{H2O2} \times N_A \times h \times c) \times 2}{S \times I \times t \times \lambda} \times 100\% \quad (2)$$

Where M is the yield of H_2O_2 (1991 x 10^{-6} mol), N_A is the Avogadro's constant (6.022 × 10^{23} mol^{-1}), h defines the Planck constant (6.626 × 10^{-34} J·s), c for the speed of light (3 × 10^8 m s^{-1}), S the irradiation area (8 cm^2), I is the intensity of the irradiation light (467 nm, 159 mW cm^{-2}), t the photoreaction time (7200 s), and λ is the wavelength of the monochromatic light (467 x 10^{-9} m). AQY was calculated for different wavelengths of light ranging from 390 nm, 440 nm, 467 nm, and 510 nm using 5 mg TTT-DTDA COF in 10 mL pure water over a period of 2 hours.

Solar-to-chemical energy conversion efficiency measurements

The solar-to-chemical energy conversion (SCC) efficiency is generally evaluated using a solar simulator as a light source during photocatalytic experiments. The power intensity of the monochromatic light is analyzed using an optical power meter. The SCC efficiency can be calculated using the following equation:

$$\text{SSC efficiency } (\%) = \frac{[\Delta G \text{ for } H_2O_2 \text{ generation } (\text{J mol}^{-1})]\,[H_2O_2 \text{ formed (mol)}]}{[\text{Total input power(W)}][\text{Reaction time (s)}]} \times 100\% \quad (3)$$

Where △G is the free energy for H_2O_2 formation (117 kJ mol^{-1}). The formed H_2O_2 (996 x 10^{-6} mol), total input power 1.272 W, and the photoreaction time (7200 s).

Synthesis of TAA-DTDA COF:

Typically, in a Pyrex tube 4,4',4"-Triaminotriphenylamine (TAA, 29 mg, 0.1 mmol) and thieno[3,2-b]thiophene-2,5-dicarbaldehyde (DTDA, 29.4 mg, 0.15 mmol) were dispersed in 2 ml

orthodichlorobenzene (*o*-DCB), 1 ml ethanol (EtOH), and 0.5 ml of 6M acetic acid. The mixture was sonicated for 10 minutes to get a homogeneous solution. It was then flash frozen at 77K in a liquid nitrogen bath and made to undergo three freeze-pump-thaw cycles. The Pyrex tube was sealed off and heated at 120 °C for three days. A dark brown precipitate was obtained, which was washed with acetone, methanol, THF, and hexane. After drying, TAA-DTDA was obtained as a dark brown powdered mass.

Synthesis of TAPB-DTDA COF:

Typically, in a Pyrex tube, 1,3,5-Tris(4-aminophenyl)benzene (TAPB, 53 mg, 0.15 mmol) and thieno[3,2-b]thiophene-2,5-dicarbaldehyde (DTDA, 45 mg, 0.229 mmol) were dispersed in 0.5 ml mesitylene, 3.5 ml dioxane, and 0.5 ml of 6M acetic acid. The mixture was sonicated for 10 minutes to get a homogeneous solution. It was then flash frozen at 77K in a liquid nitrogen bath and made to undergo three freeze-pump-thaw cycles. The Pyrex tube was sealed off and heated at 120 °C for three days. A yellow precipitate was obtained, which was washed with acetone, methanol, THF, and hexane. After drying, TAPB-DTDA was obtained as a yellow powdered mass.

Synthesis of TTT-DTDA COF:

Typically, in a Pyrex tube 4,4',4"-(1,3,5-triazine-2,4,6 triyl)trianiline (TTT, 53 mg, 0.15 mmol) and thieno[3,2-b]thiophene-2,5-dicarbaldehyde (DTDA, 45 mg, 0.229 mmol) was dispersed in 1 ml mesitylene, 3.5 ml dioxane and 0.5 ml of 6 M acetic acid. The mixture was sonicated for 10 minutes to get a homogeneous solution. It was then flash frozen at 77K in a liquid nitrogen bath and made to undergo three freeze-pump-thaw cycles. The Pyrex tube was sealed off and heated at 120 °C for three days. An orange-yellow precipitate was obtained, which was washed with acetone, methanol, THF, and hexane. After drying, TTT-DTDA was obtained as a yellow powdered mass.

Synthesis of extTTT-DTDA COF:

A Pyrex tube was charged with 4',4''',4''''''-(1,3,5-triazine-2,4,6-triyl)tris(([1,1'-biphenyl]-4-amine)) (extTTT-NH_2, 44 mg, 0.075 mmol) and thieno[3,2-b]thiophene-2,5-dicarbaldehyde (DTDA, 22 mg, 0.229 mmol) and dispersed in 1 ml *o*-DCB, 2 ml ethanol and 0.5 ml of 6 M acetic acid. The mixture was sonicated for 10 minutes to get a homogeneous solution. It was then flash frozen at

77K in a liquid nitrogen bath and made to undergo three freeze-pump-thaw cycles. The Pyrex tube was sealed off and heated at 120 °C for three days. A dark yellow precipitate was obtained, which was washed with acetone, methanol, THF, and hexane. After drying, extTTT-DTDA was obtained as a dark yellow powdered mass.

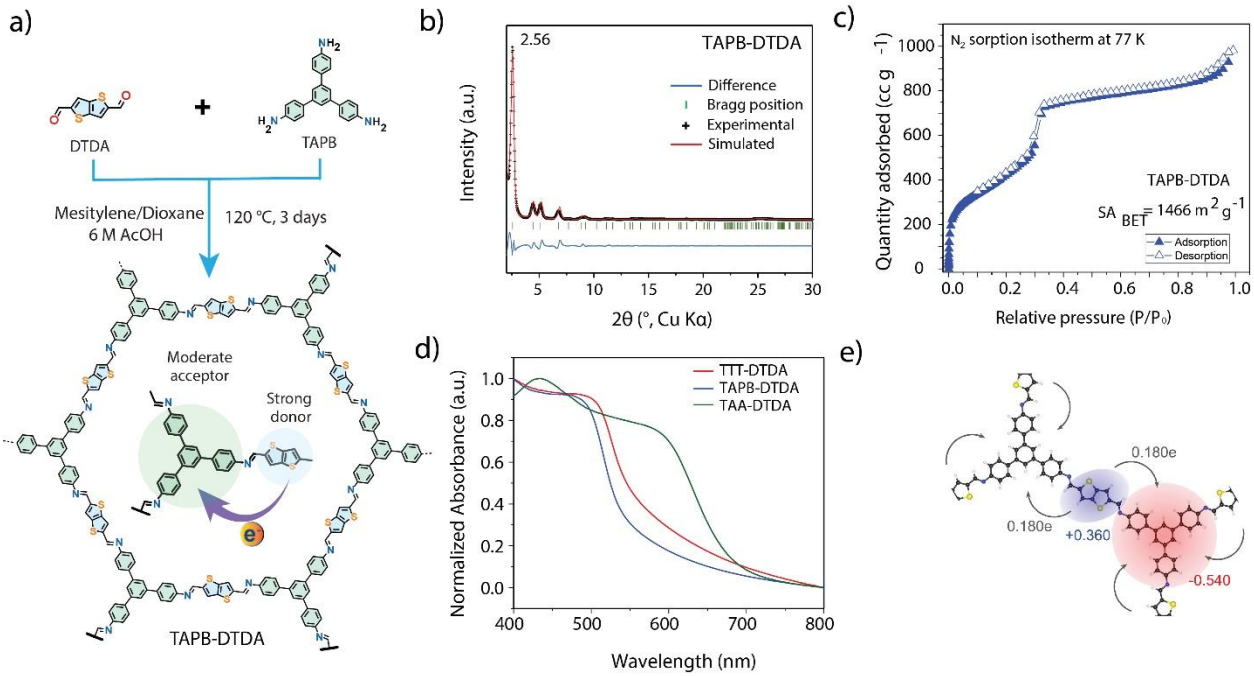

Figure S1. (a) Scheme of the synthesis of TAPB-DTDA COF from its precursors. (b) Comparison of simulated and experimental PXRD patterns of TAPB-DTDA COF. (c) N_2 sorption isotherm of TAPB-DTDA COF. (d) Solid UV-Vis spectra of the TAA-DTDA, TAPB-DTDA and TTT-DTDA COFs. (e) Partial charge distribution profile of TAPB-DTDA COF.

Section S2. Structure modelling and atomic coordinates of COFs:

A structural model of TAA-DTDA, TAPB-DTDA, TTT-DTDA and extTTT-DTDA COFs was generated with the Materials Studio programs. Theoretical parameters of the initial unit cell dimension were applied. The atomic positions and total energies were fully optimized using the Forcite module program of Materials Studio. The final crystal structure was optimized using the Dmol3 module program of Materials Studio software. Fractional atomic coordinates for the crystal structure are shown in Tables S1-S3. XRD simulation was carried out by Reflex Tools, and Cu source radiation was applied with a 0.02 step width.

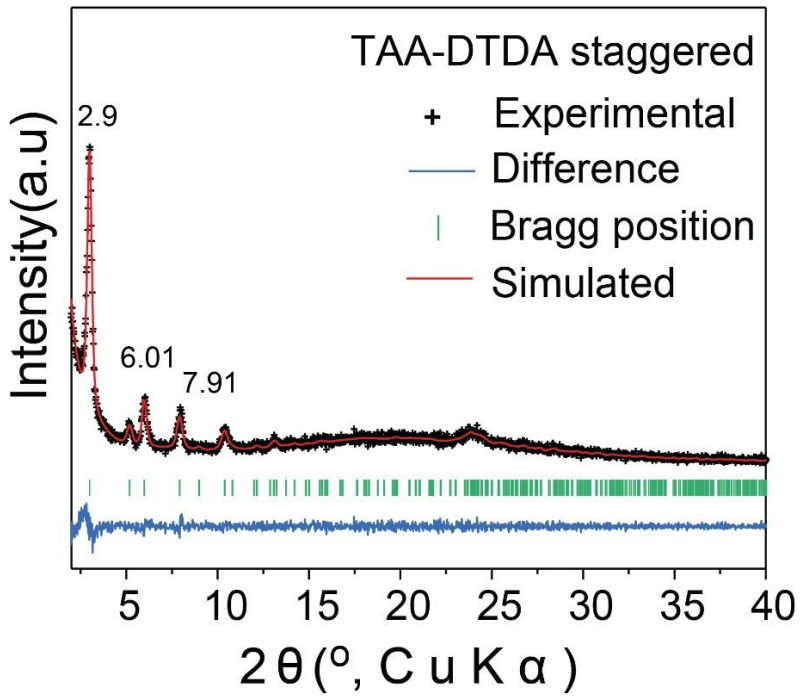

Figure S2. Comparison of experimental and simulated PXRD patterns of TAA-DTDA (staggered).

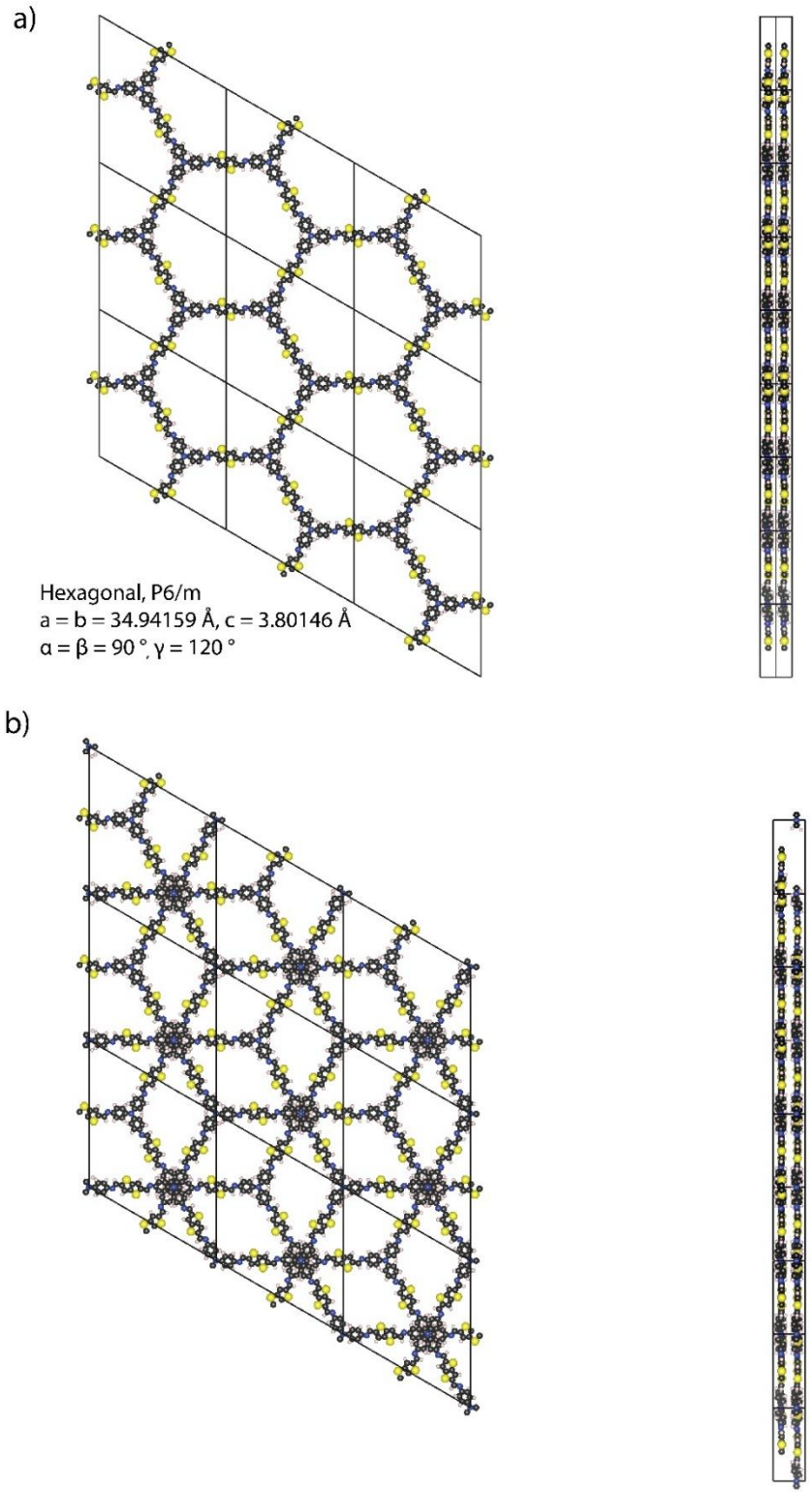

Figure S3. The simulated structures of TAA-DTDA in (a) eclipsed, and (b) staggered form.

Table S1. Fractional atomic coordinates for TAA-DTDA COF.

Space Group: P6 (168).

a = b = 34.94159 Å, c = 3.80146 Å.

α = β = 90 °, γ = 120 °.

Volume = 4019.45 $Å^3$.

Coordinates

Element	Name	a	b	c
C	C1	0.458294	0.579123	0.489334
C	C2	0.398441	0.591409	0.459963
C	C3	0.35655	0.57474	0.304554
C	C4	0.33589	0.599682	0.291803
C	C5	0.355367	0.641896	0.445232
C	C6	0.396934	0.658267	0.6062
C	C7	0.418303	0.633936	0.610535
C	C8	0.474891	0.549077	0.511554
C	C9	0.44994	0.503201	0.517544
C	C10	0.522922	0.515695	0.522448
H	H1	0.303846	0.586137	0.165594
H	H2	0.482762	0.614863	0.485206
H	H3	0.341354	0.542057	0.184476
H	H4	0.412382	0.690445	0.732631
H	H5	0.449637	0.647029	0.75045
H	H6	0.414032	0.485927	0.513504
N	N2	0.416194	0.563805	0.465423
N	N1	0.333333	0.666667	0.443793
S	S1	0.531679	0.568718	0.517265

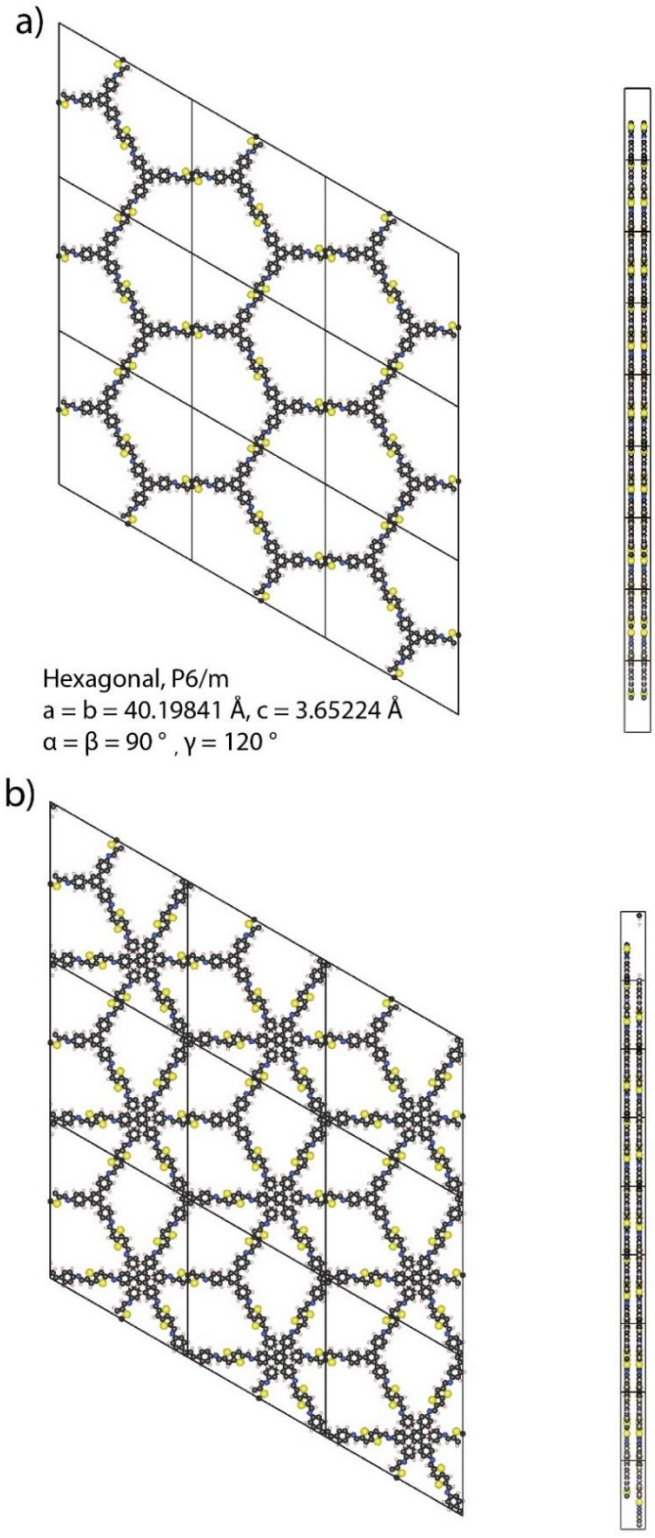

Figure S4. The simulated structures of TAPB-DTDA in (a) eclipsed, and (b) staggered form.

Table S2. Fractional atomic coordinates for TAPB-DTDA COF.

Space Group: P6 (168).

a = b = 40.19841 Å, c = 3.65224 Å.

α = β = 90 °, γ = 120 °.

Volume = 5111.02 $Å^3$.

Coordinates

Element	Name	a	b	c
C	C1	0.352144	0.707291	0.499941
C	C2	0.311984	0.685059	0.499942
C	C3	0.371714	0.749705	0.499948
C	C4	0.412104	0.772419	0.50068
C	C5	0.430667	0.812118	0.500699
C	C6	0.4096	0.831501	0.500023
C	C7	0.369338	0.809115	0.499346
C	C8	0.350994	0.769378	0.499269
C	C9	0.461626	0.894749	0.500012
C	C10	0.476287	0.935242	0.500077
C	C11	0.514621	0.964237	0.500085
C	C12	0.48202	0.999243	0.500107
H	H1	0.429724	0.758827	0.501313
H	H2	0.461993	0.82815	0.501316
H	H3	0.353044	0.824131	0.498861
H	H4	0.319705	0.753456	0.498652
H	H5	0.48352	0.88576	0.499903
H	H6	0.538353	0.958452	0.500071
H	H7	0.295287	0.699514	0.499947
N	N1	0.424985	0.871128	0.500034
S	S1	0.444284	0.952617	0.500102

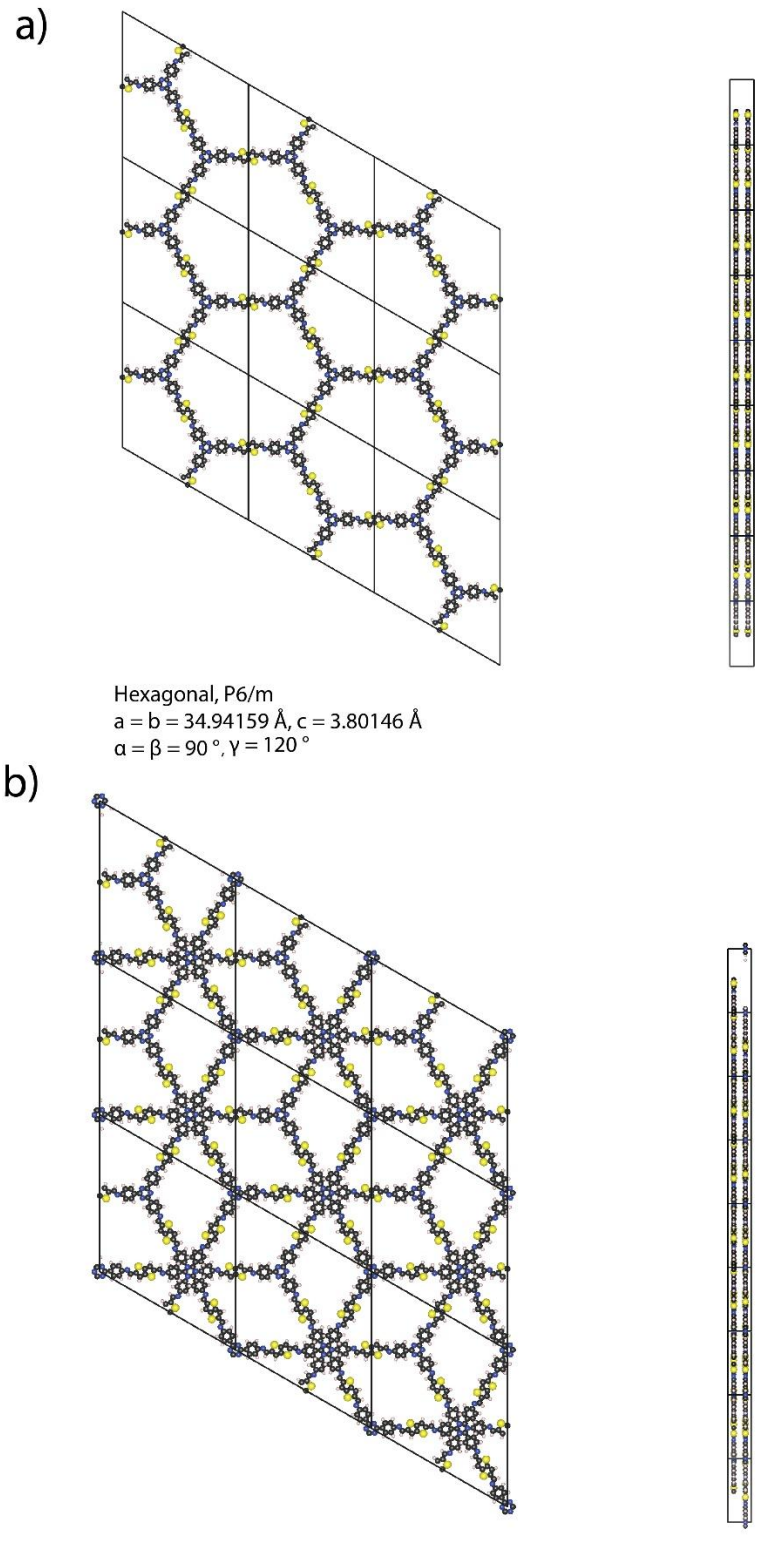

Figure S5. Simulated structures of (a) eclipsed TTT-DTDA, and (b) staggered TTT-DTDA.

Table S3. Fractional atomic coordinates for TTT-DTDA COF.

Space Group: P6 (168).

a = b = 39.68472 Å, c = 3.63371 Å.

α = β = 90 °, γ = 120 °.

Volume = 4955.96 $Å^3$.

Coordinates

Element	Name	a	b	c
C	C1	0.351039	0.704837	0.500000
C	C2	0.370745	0.74753	0.500000
C	C3	0.411589	0.769776	0.500000
C	C4	0.430187	0.80996	0.500000
C	C5	0.408452	0.829263	0.500000
C	C6	0.36758	0.806764	0.500000
C	C7	0.348969	0.766527	0.500000
C	C8	0.461014	0.893424	0.500000
C	C9	0.475794	0.934409	0.500000
C	C10	0.514664	0.963688	0.500000
C	C11	0.481797	0.999283	0.500000
H	H1	0.428107	0.754604	0.500000
H	H2	0.4619	0.826502	0.500000
H	H3	0.351288	0.822172	0.500000
H	H4	0.317359	0.748851	0.500000
H	H5	0.483227	0.884396	0.500000
H	H6	0.538608	0.957711	0.500000
N	N1	0.31189	0.685187	0.500000
N	N2	0.423901	0.869435	0.500000
S	S1	0.443469	0.952104	0.500000

.

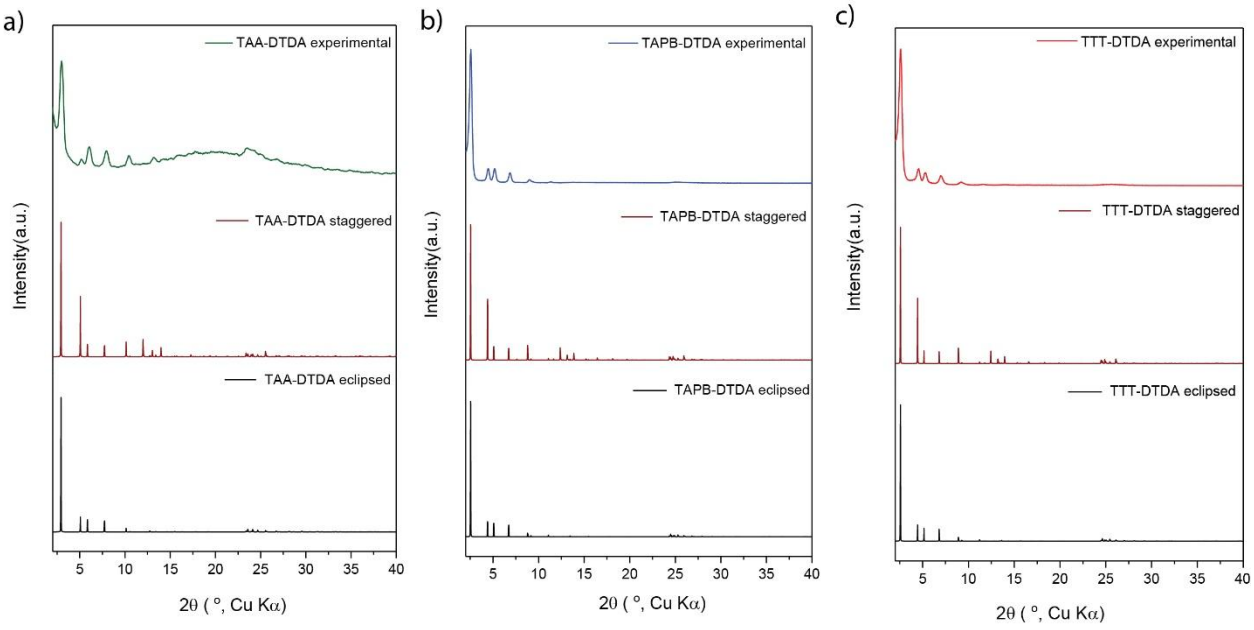

Figure S6. Comparison between the simulated and experimental PXRD patterns of (a) TAA-DTDA, (b) TAPB-DTDA, and (c) TTT-DTDA COFs, showing good agreement between experimental and eclipsed patterns.

Section S3. Characterization of COFs:

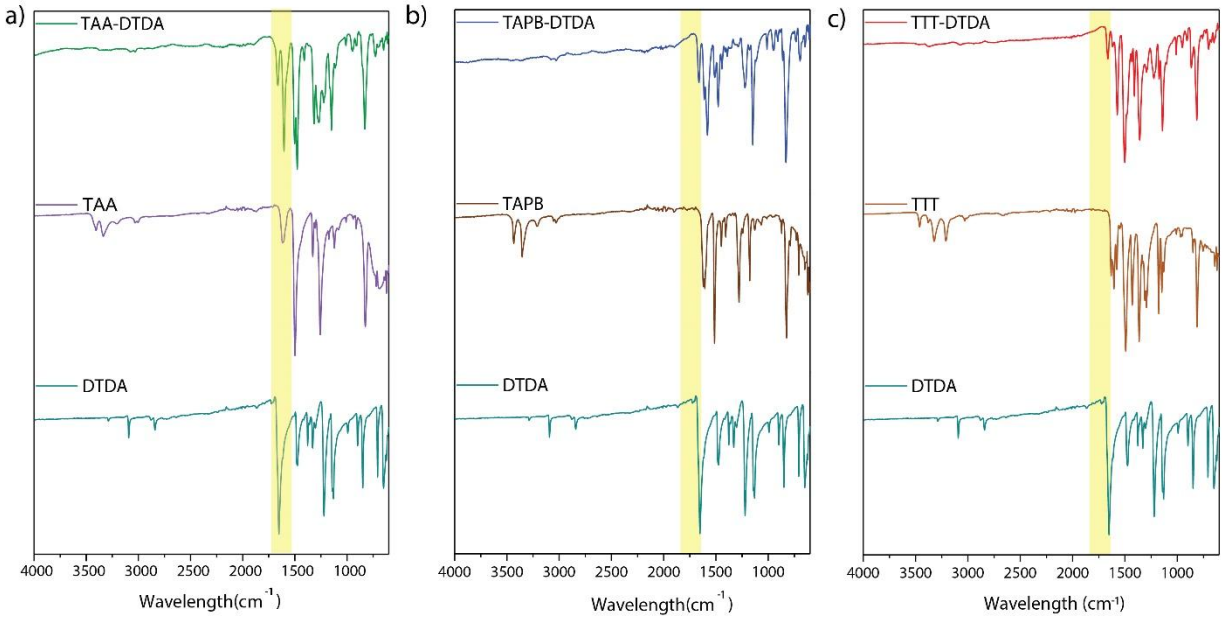

Figure S7. FT-IR analysis of the precursors and COF (a) TAA-DTDA, (b) TAPB-DTDA, and (c) TTT-DTDA COF along with their precursors.

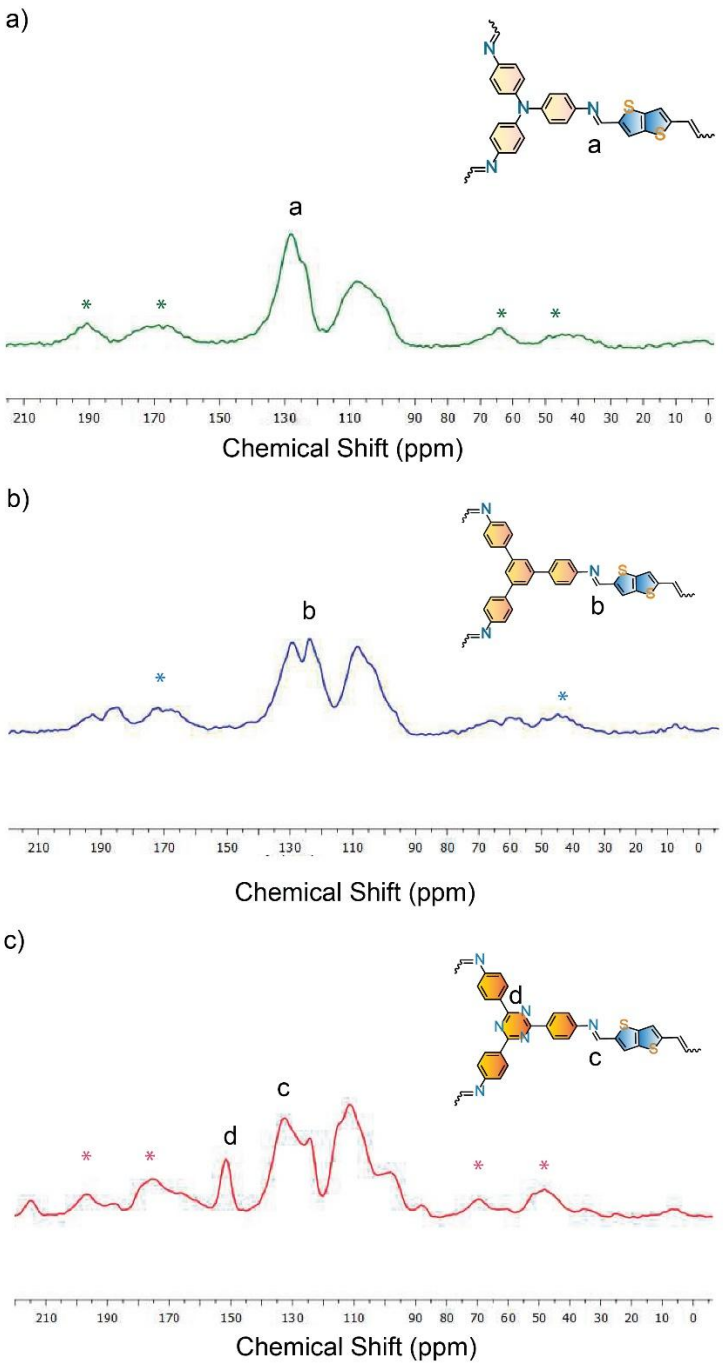

Figure S8. Solid-state ^{13}C CP-MAS NMR analyses of (a) TAA-DTDA, (b) TAPB-DTDA, (c) TTT-DTDA COFs.

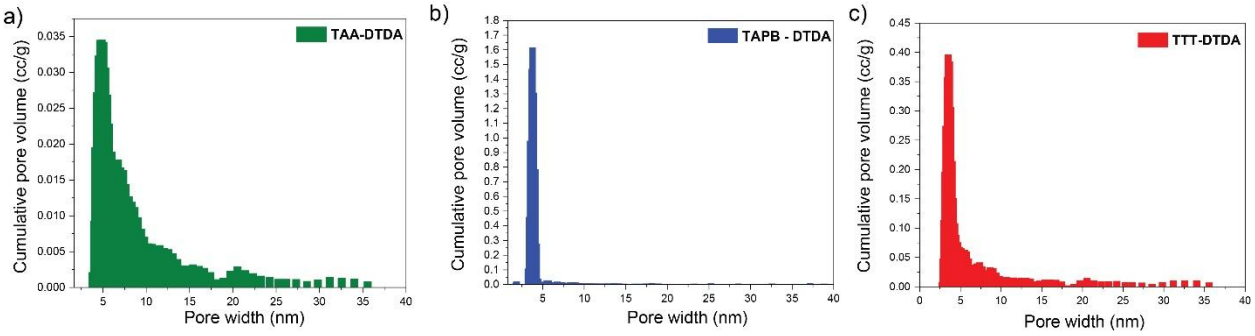

Figure S9. Pore size distribution of the COFs calculated using Density Functional Theory for (a) TAA-DTDA, (b) TAPB-DTDA, and (c) TTT-DTDA COFs.

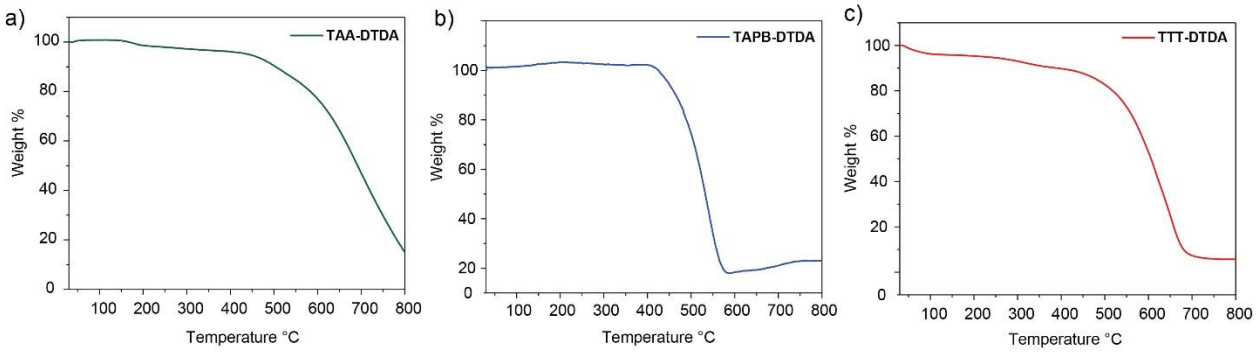

Figure S10. Thermogravimetric analysis profiles of (a) TAA-DTDA, (b) TAPB-DTDA, and (c) TTT-DTDA COFs.

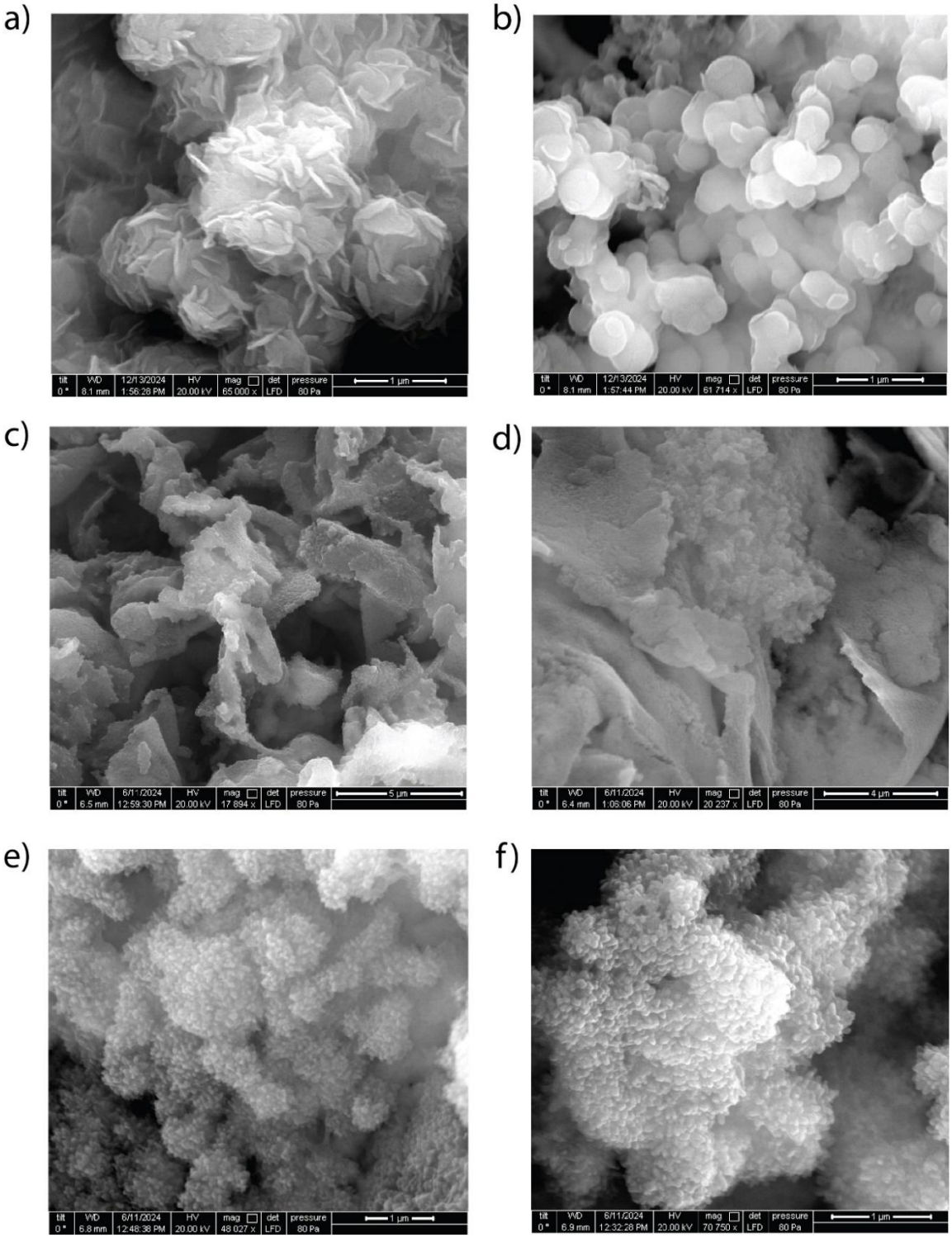

Figure S11. FE-SEM images of (a, b) TAA-DTDA, (c, d) TAPB-DTDA, and (e, f) TTT-DTDA COFs.

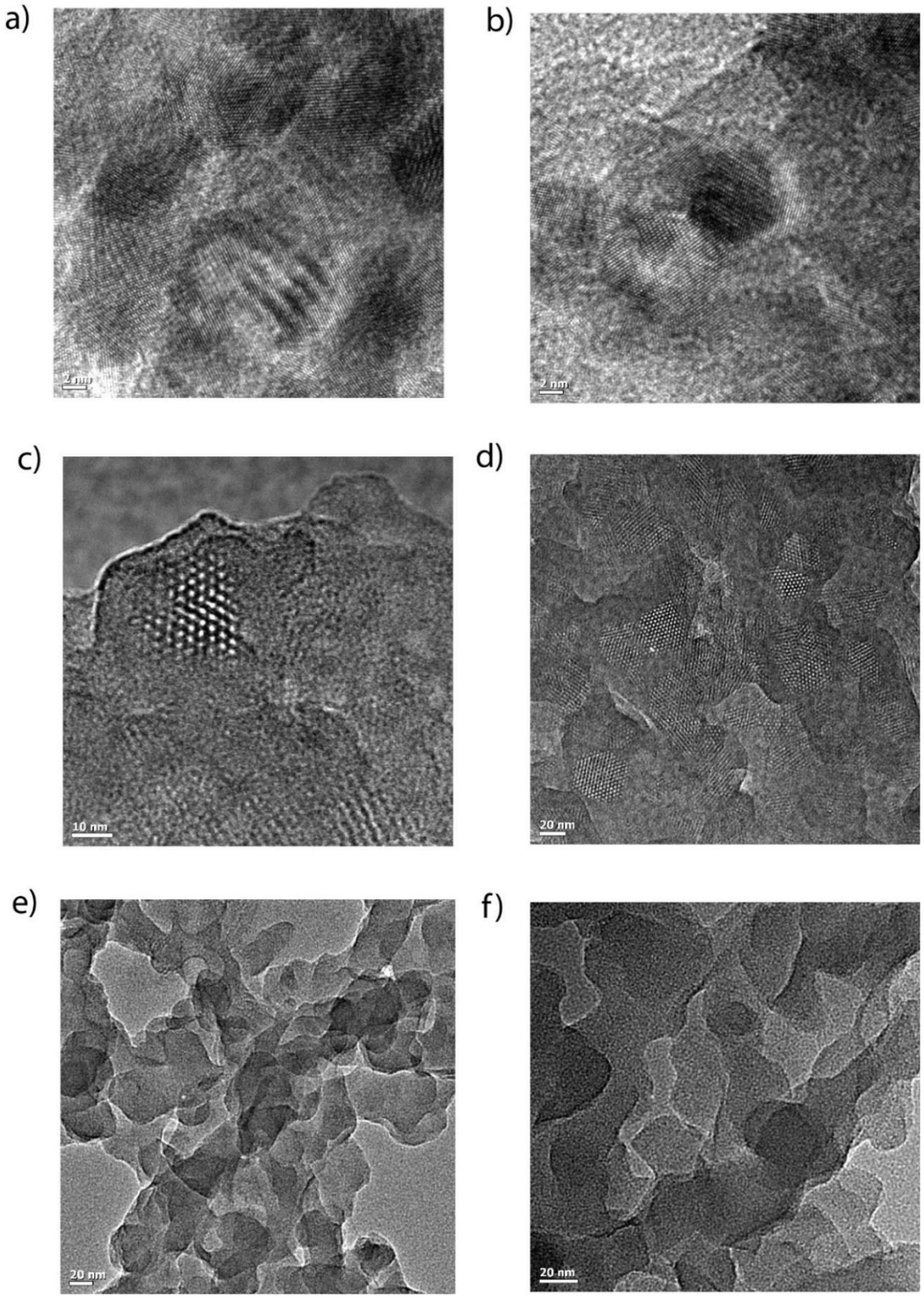

Figure S12. HR-TEM images of (a, b) TAA-DTDA, (c. d) TAPB-DTDA, and (e, f) TTT-DTDA COFs.

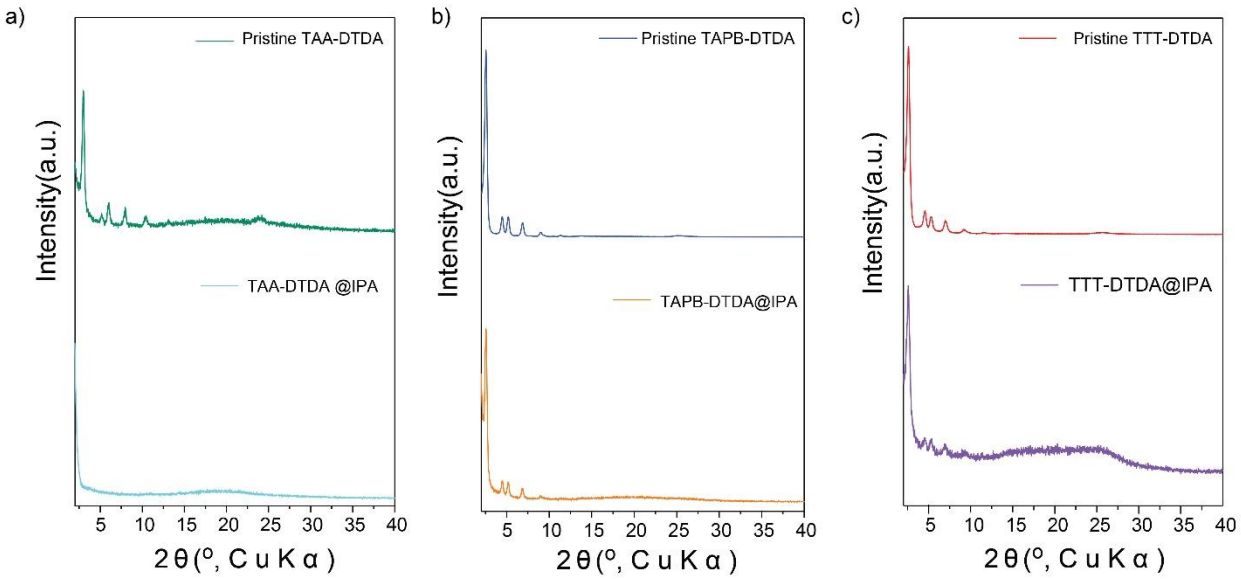

Figure S13. PXRD patterns of pristine COF and after immersion in benzyl alcohol for 12 hours for (a) TAA-DTDA, (b) TAPB-DTDA, and (c) TTT-DTDA COF.

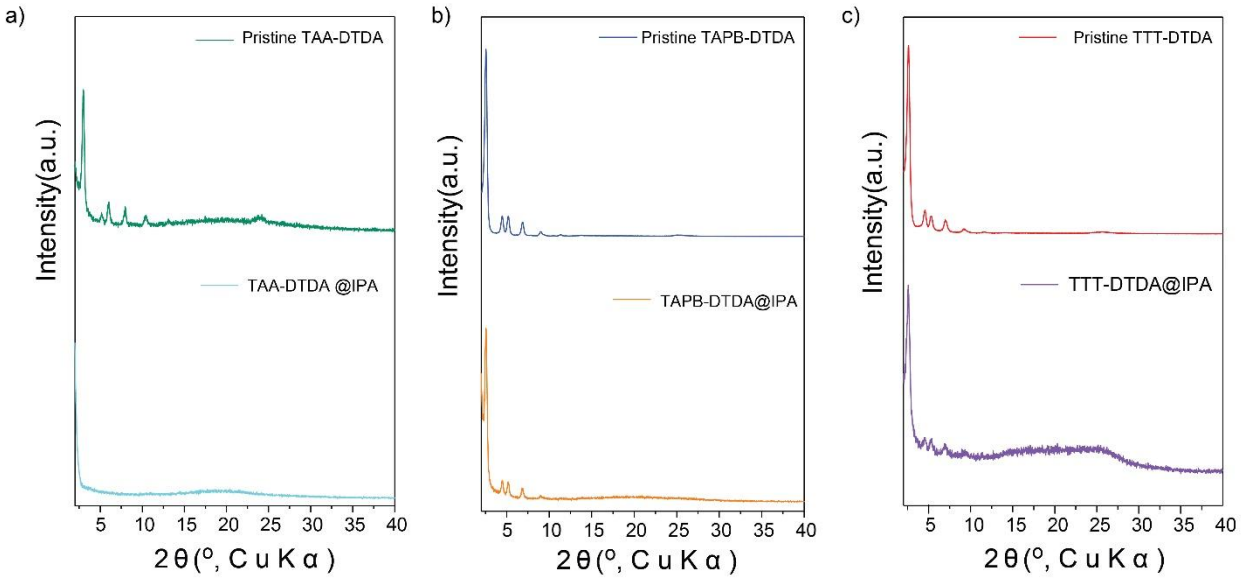

Figure S14. PXRD patterns of pristine COF and after immersion in isopropyl alcohol for 12 hours for (a) TAA-DTDA, (b) TAPB-DTDA, and (c) TTT-DTDA COF.

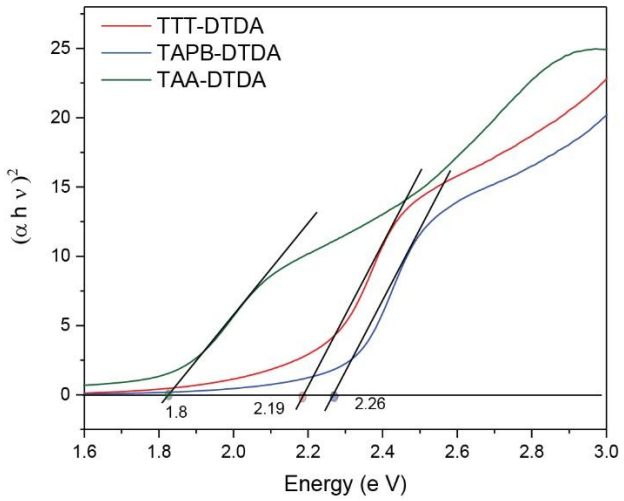

Figure S15. Tauc plot for the determination of the band gap of the COFs.

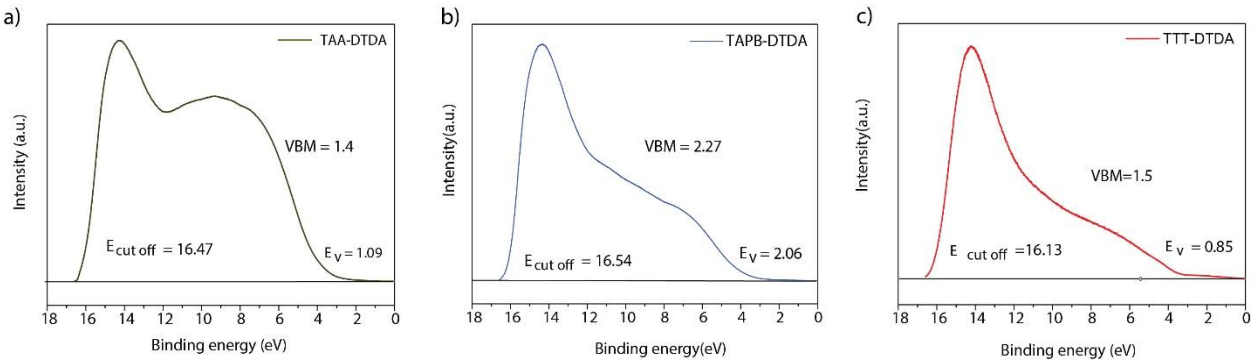

Figure S16. UPS analyses of (a) TAA-DTDA, (b) TAPB-DTDA, (c) TTT-DTDA COFs.

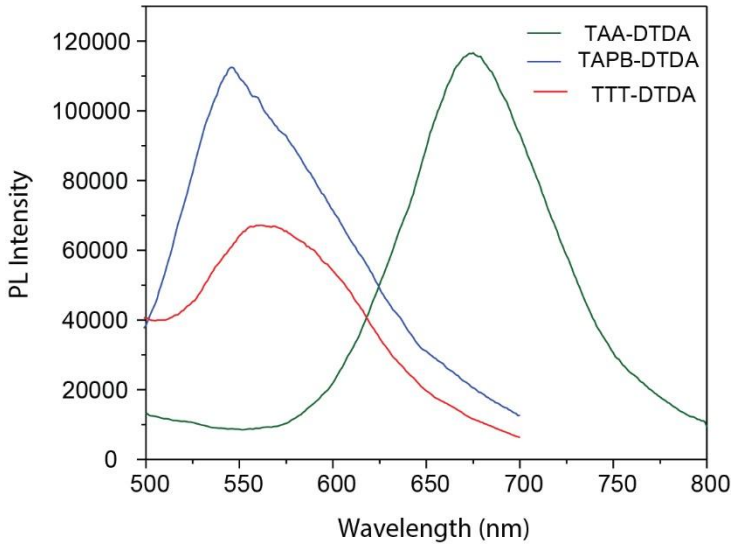

Figure S 17. Solid-state photoluminescence analyses of the COFs.

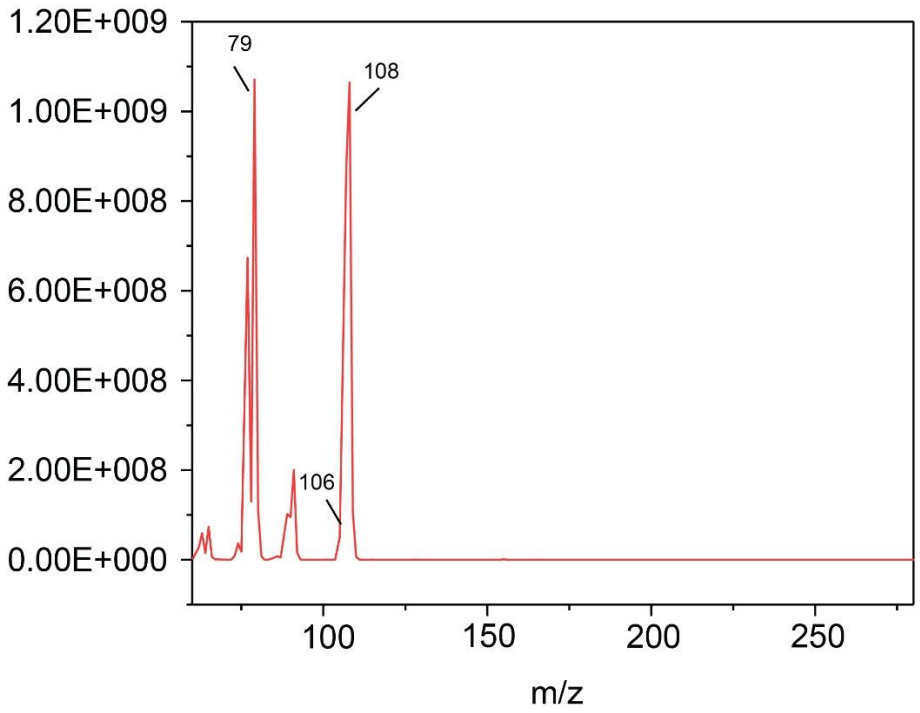

Figure S18. Mass spectra of an aliquot collected from the photocatalytic reaction mixture using TTT-DTDA.

Section S4. Electrochemical measurements:

The electrochemical experiments were carried out in a three-electrode beaker cell. An Ag/AgCl reference electrode, a platinum wire counter electrode, and 0.5 N Na_2SO_4 aqueous electrolyte were used in this matter. The electrochemical performance of the samples was determined by the CHI660E electrochemical workstation (CHI Instruments, USA). The catalyst ink was prepared using 5 mg of COF sample in 90 μL Milli-Q water, 100 μL of isopropyl alcohol (IPA), and 10 μL of Nafion binder (5 wt.% in alcohol). The solution or suspension was sonicated for half an hour till a homogeneous solution was obtained.

Photocurrent measurement

The experimental procedure includes 30 μL of the same ink deposited onto an ITO glass substrate and left to dry overnight. The photocurrent responses were measured over 5 cycles of 10-second sequential light "On/Off" cycles with a 300 W Xenon arc lamp, used as the illumination source.

Mott-Schottky Analysis

15 μL of that solution was drop cast onto a Glassy Carbon electrode (3 mm diameter) and left overnight for drying, hence to be used as the working electrode. Three alternative frequencies (i.e., 500 Hz, 750 Hz, and 1000 Hz) were used for the Mott-Schottky analysis, and the corresponding potential window was 1.5 to -1.5 V.

Electrochemical Impedance Spectroscopy (EIS): EIS measurements were done on the same ITO-fabricated electrode above. The EIS spectra were recorded at 0 V to the reference electrode. The frequency range was from 1000 kHz to 50 mHz. The experiments were done in the presence and absence of the light source mentioned earlier to check the effect of light irradiation on the charge transfer resistance (R_{ct}) of the sample.

Rotating ring-disk electrode (RRDE) measurements: A ring-disk electrode (RRDE-3A Rotating Ring Disk Electrode Apparatus Ver.2.0) served as the substrate for the working electrode. A RRDE electrode with a glassy carbon electrode (0.248 cm^2) and a platinum ring electrode was used as the working electrode (0.187 cm^2). The working electrode was prepared as RDE measurements. The voltammograms were obtained in a 0.1 M KOH at room temperature under the protection of an Ar or O_2 atmosphere with a scan rate of 10 mV s^{-1} and a rotation rate of 1600 rpm. The potential of the ring electrode was set to -0.23 and 0.6 V (vs. Ag/AgCl) to detect O_2 or H_2O_2, respectively.

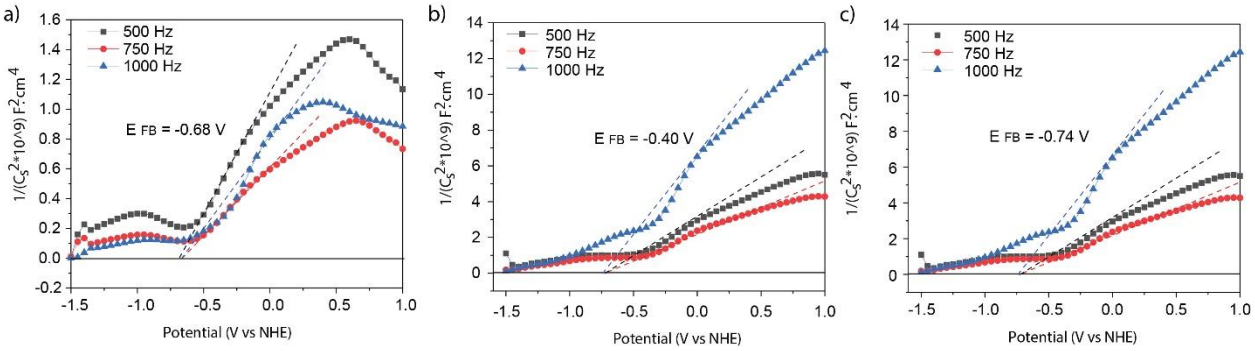

Figure S19. Mott Schottky plots of (a) TAA-DTDA, (b) TAPB-DTDA, (c) TTT-DTDA COFs.

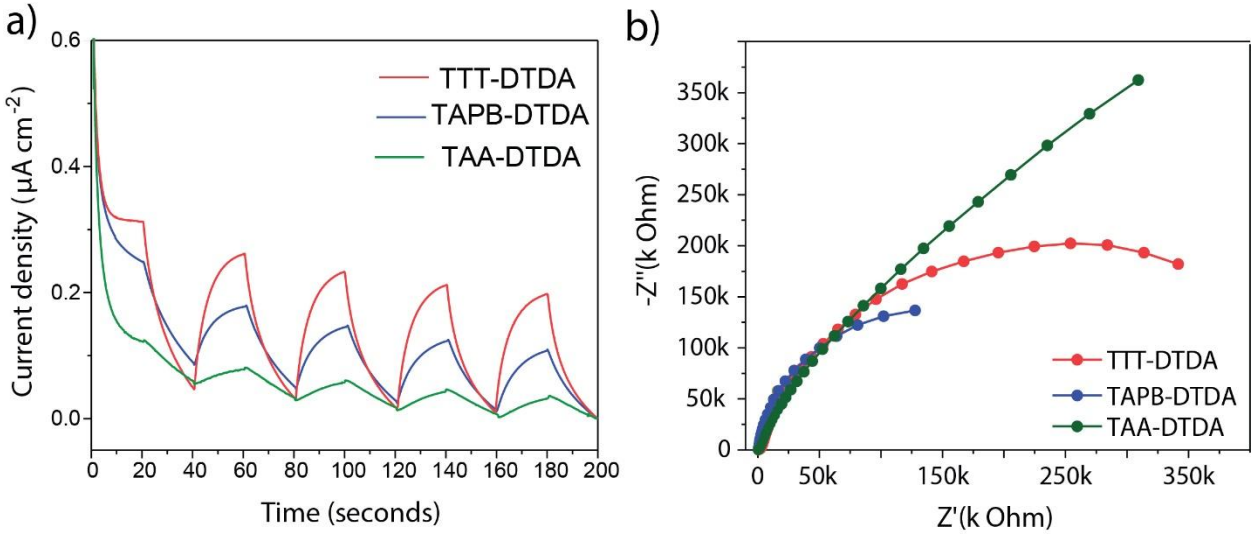

Figure S20. (a) Photocurrent measurements for TAA-DTDA, TAPB-DTDA, and TTT-DTDA COFs. (b) EIS Nyquist plots of TAA-DTDA, TAPB-DTDA, and TTT-DTDA COFs.

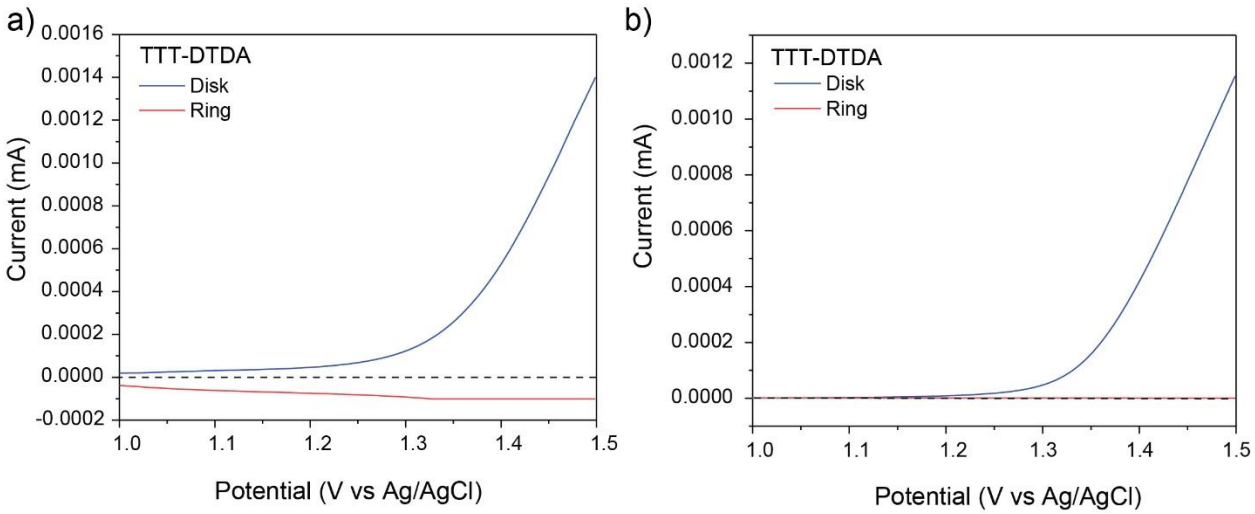

Figure S21. (a) RRDE voltammograms of TTT-DTDA COF. The potential of the Pt ring electrode is set at -0.23 V versus Ag/AgCl to detect O_2. (b) RRDE voltammograms of TTT-DTDA COF. The potential of the Pt ring electrode is set to 0.6 V versus Ag/AgCl to detect H_2O_2. The WOR pathway towards H_2O_2 generation, the generated O_2 molecules can participate in the production of H_2O_2 via the $4e^-$–$2e^-$ cascaded process ($H_2O \rightarrow O_2 \rightarrow H_2O_2$)].

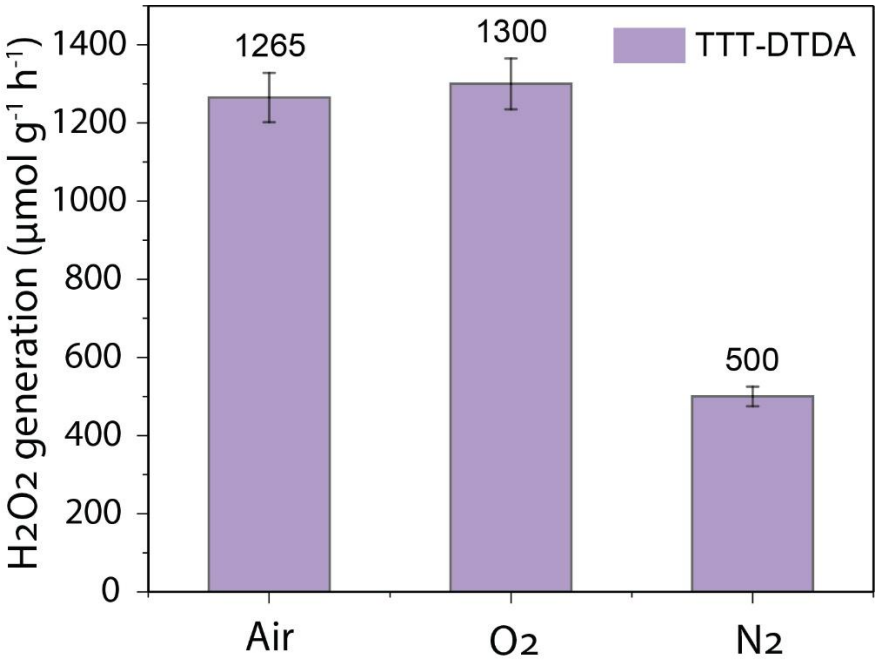

Figure S22. Photocatalytic H_2O_2 generation under different gas purging conditions.

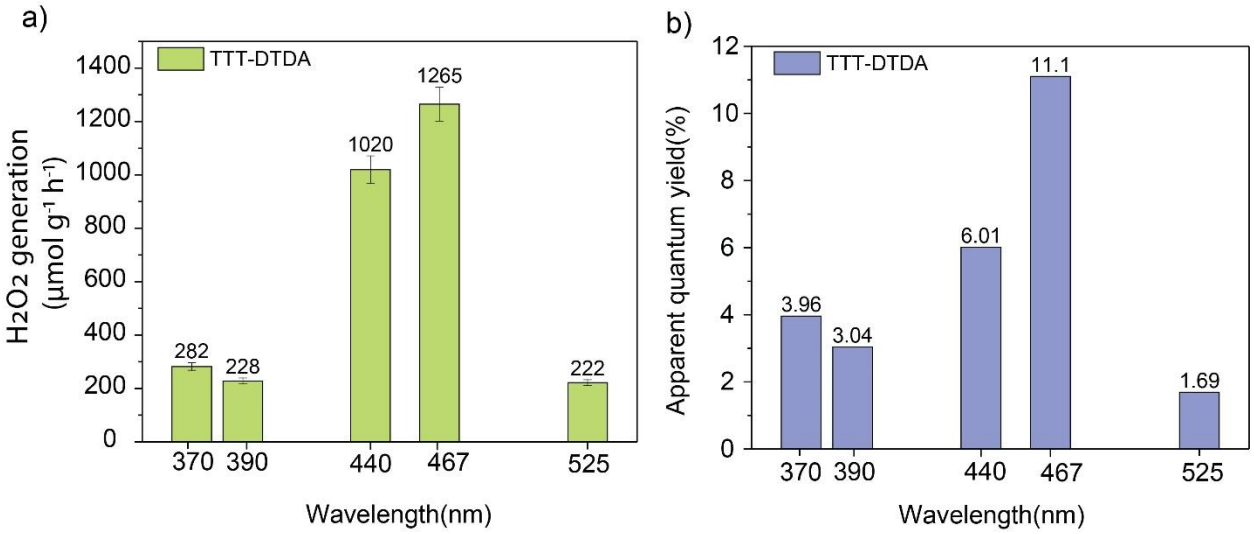

Figure S23. (a) Photocatalytic H_2O_2 generation rates in pure water using TTT-DTDA COF at different wavelengths. (b) Apparent quantum yield (AQY) measured at different wavelengths using TTT-DTDA COF.

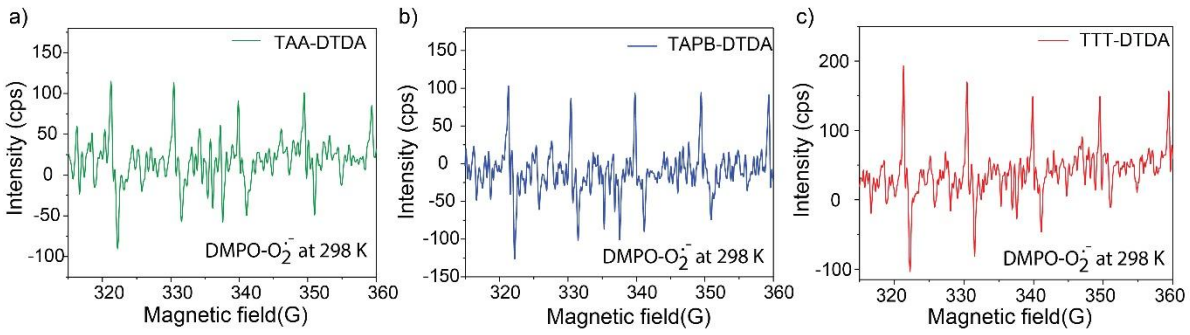

Figure S24. EPR spectra of DMPO-O_2 •- adduct of (a) TAA-DTDA, (b) TAPB-DTDA, and (c) TTT-DTDA COFs collected at 298 K showing the hyperfine splitting pattern in an EPR spectrum.

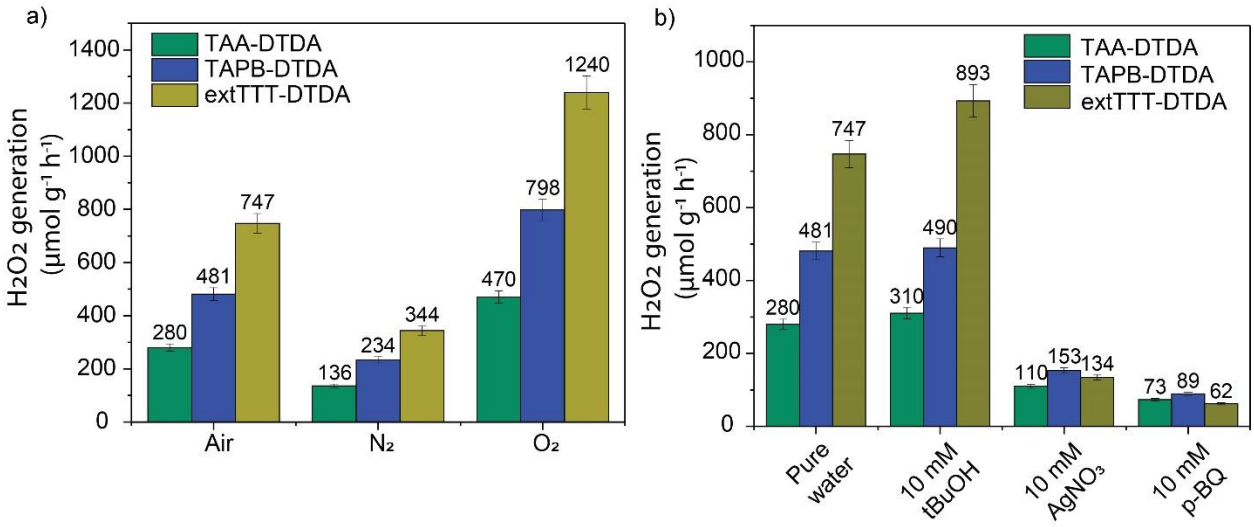

Figure S25. Photocatalytic H_2O_2 generation using TAA-DTDA, TAPB-DTDA, and extTTT-DTDA COFs under (a) different atmospheres, and (b) in the presence of different scavengers.

Section S5. Characterization and application of extTTT-DTDA COF:

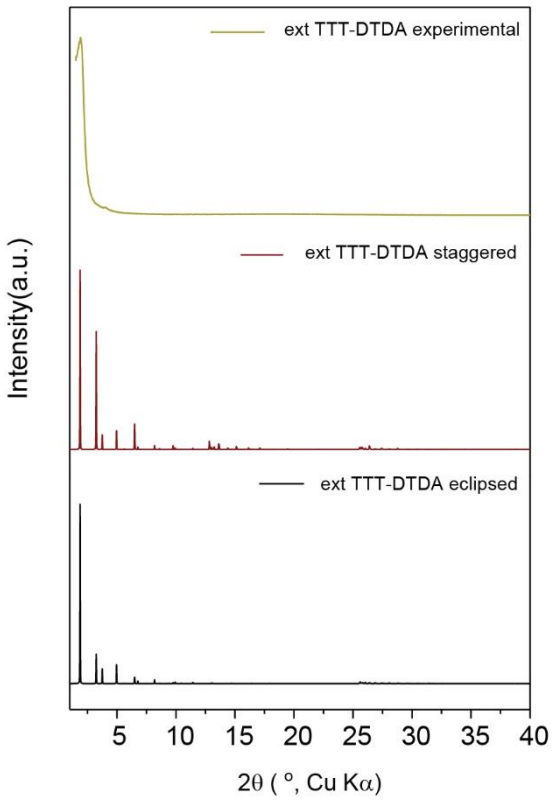

Figure S26. Comparison between simulated and experimental PXRD patterns showing good agreement between experimental and eclipsed patterns for extTTT-DTDA COF.

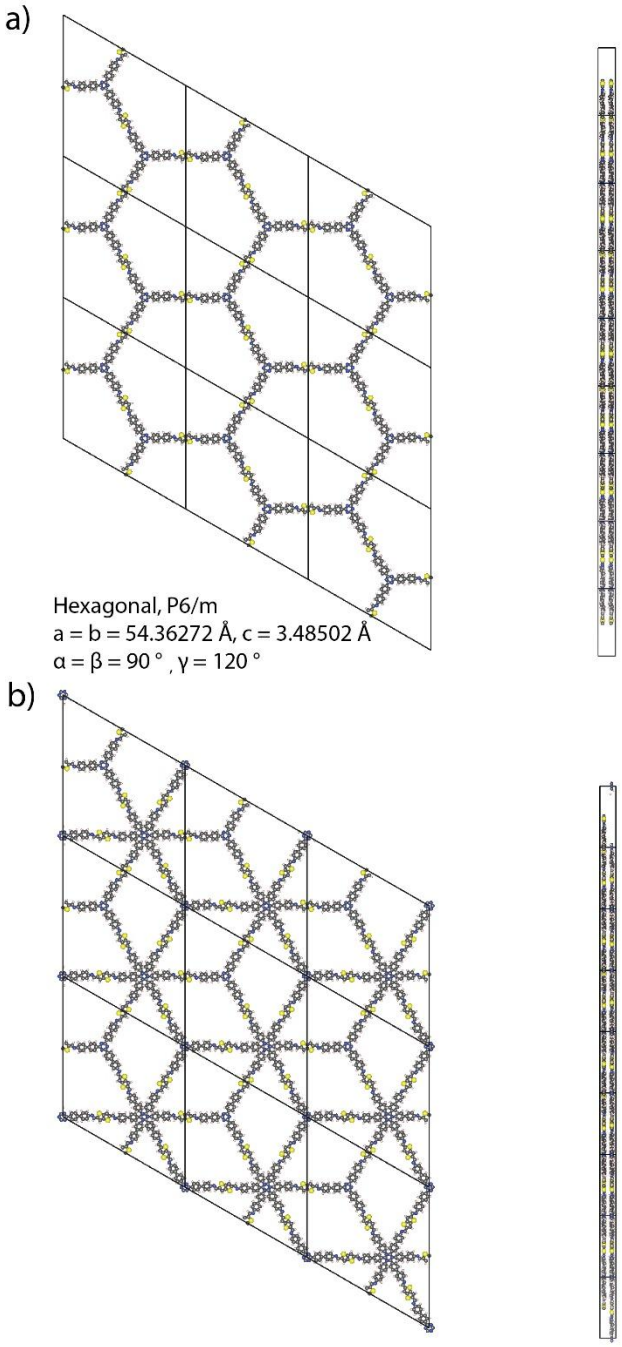

Figure S27. Simulated structures of (a) eclipsed extTTT-DTDA, and (b) staggered extTTT-DTDA COFs.

Table S4. Fractional atomic coordinates of extTTT-DTDA COF.

Space Group: P6 (168).

a = b = 54.36272 Å, c = 3.48502 Å.

α = β = 90 °, γ = 120 °.

Volume = 8919.45 $Å^3$.

Coordinates

Element	Name	a	b	c
C	C1	0.34631	0.694509	0.491785
C	C2	0.402772	0.816235	0.502393
C	C3	0.431168	0.832515	0.381925
C	C4	0.444829	0.861876	0.378296
C	C5	0.430506	0.876063	0.501056
C	C6	0.401985	0.85987	0.616259
C	C7	0.388442	0.830493	0.618065
C	C8	0.469629	0.922013	0.517588
C	C9	0.481378	0.952053	0.508213
C	C10	0.509902	0.972895	0.50711
C	C11	0.486879	-0.000194	0.501377
C	C12	0.364836	0.639201	0.492839
C	C13	0.393797	0.654213	0.399856
C	C14	0.40948	0.640509	0.401644
C	C15	0.396772	0.61162	0.499237
C	C16	0.367734	0.596794	0.592916
C	C17	0.351889	0.610333	0.588528
H	H1	0.442158	0.821724	0.274766
H	H2	0.466387	0.873961	0.265691

H	H3	0.391254	0.871229	0.710337
H	H4	0.366539	0.818192	0.717839
H	H5	0.484952	0.914325	0.541166
H	H6	0.527078	0.968083	0.510498
H	H7	0.403342	0.676525	0.320518
H	H8	0.431792	0.651989	0.31678
H	H9	0.357833	0.574553	0.679213
H	H10	0.329438	0.599137	0.664756
N	N1	0.317741	0.680272	0.491828
N	N2	0.442431	0.905365	0.505954
S	S1	0.458429	0.965697	0.501556

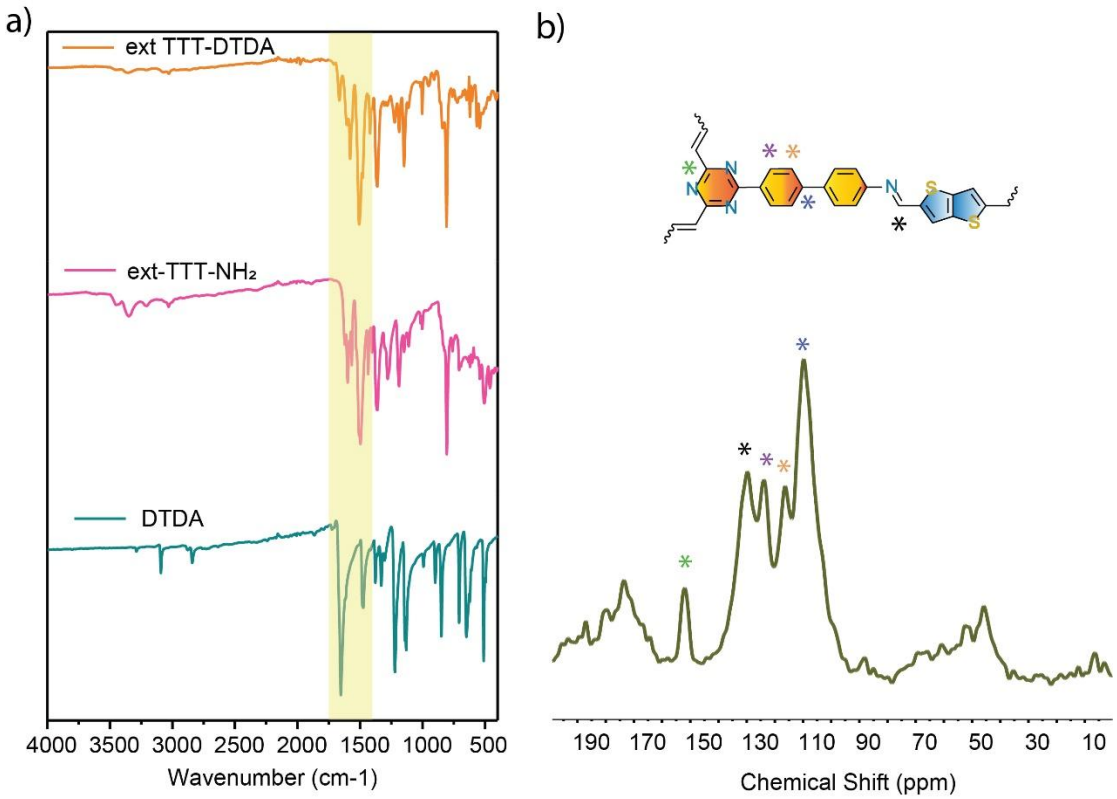

Figure S28. (a) FT-IR spectra of extTTT-DTDA along with precursors. (b) Solid state ^{13}C-NMR of extTTT-DTDA COF.

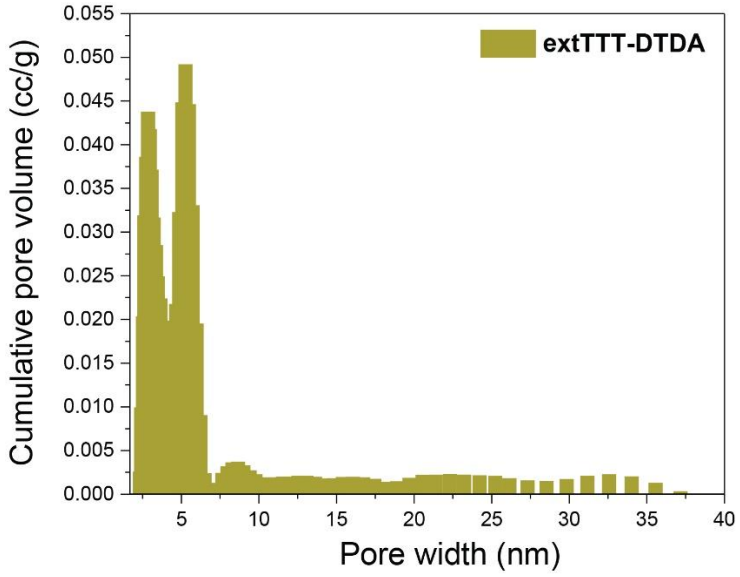

Figure S29. Pore size distribution of extTTT-DTDA COF.

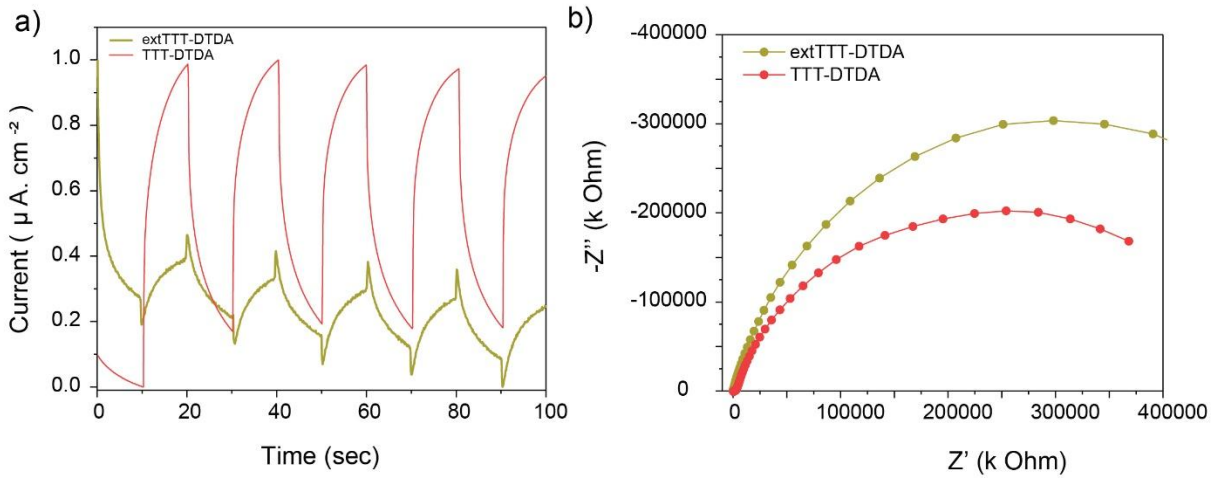

Figure S30. (a) Transient photocurrent responses of extTTT-DTDA in comparison to TTT-DTDA COFs. (b) EIS Nyquist plots of TTT-DTDA and extTTT-DTDA COFs.

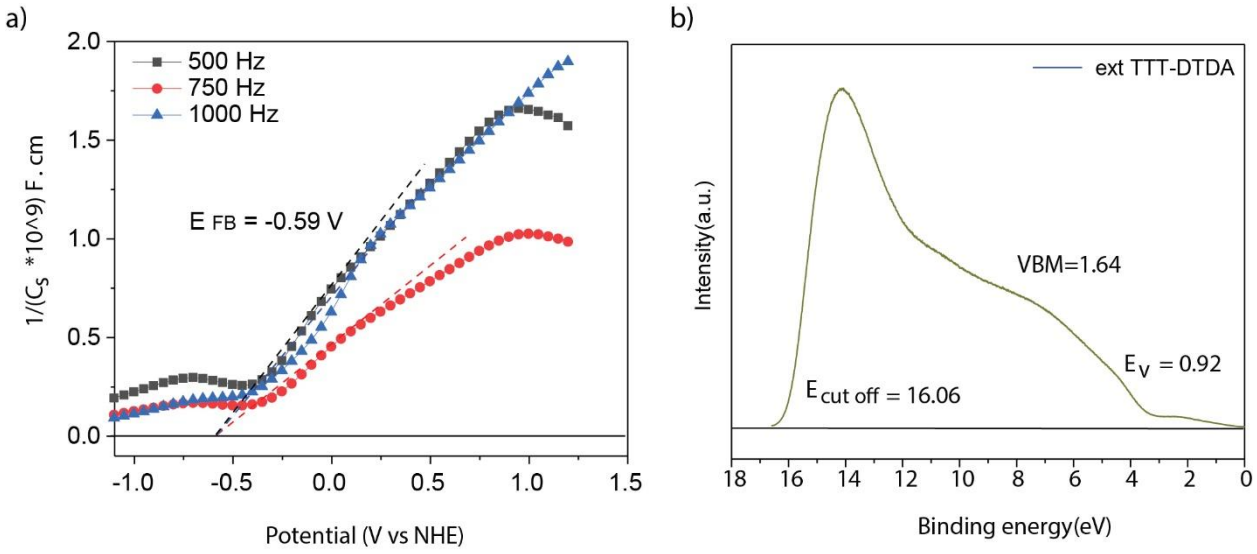

Figure S31. (a) Mott-Schottky analysis of extTTT-DTDA COF. (b) Ultraviolet photoelectron spectroscopy (UPS) spectrum of extTTT-DTDA COF.

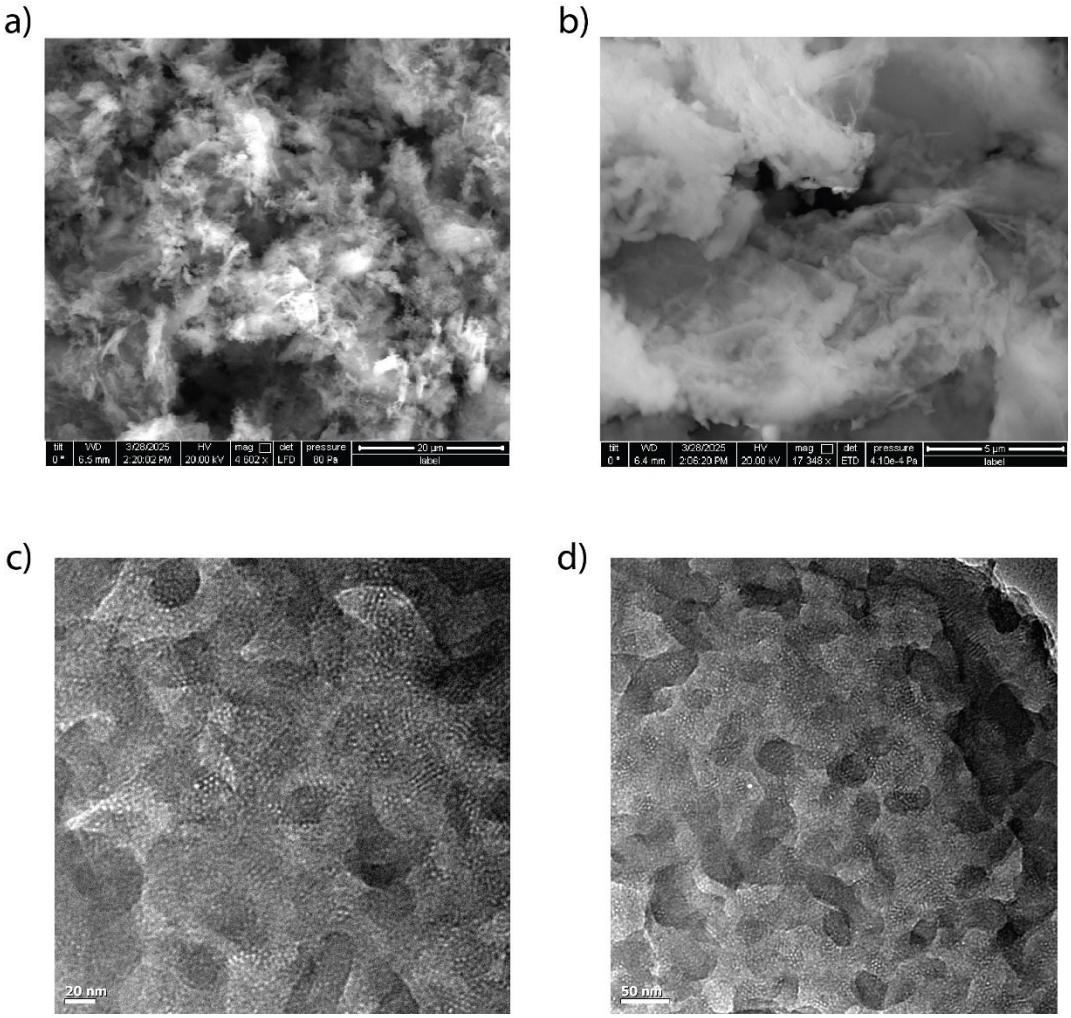

Figure S32. (a, b) FE-SEM, and (c, d) HR-TEM images of extTTT-DTDA COF.

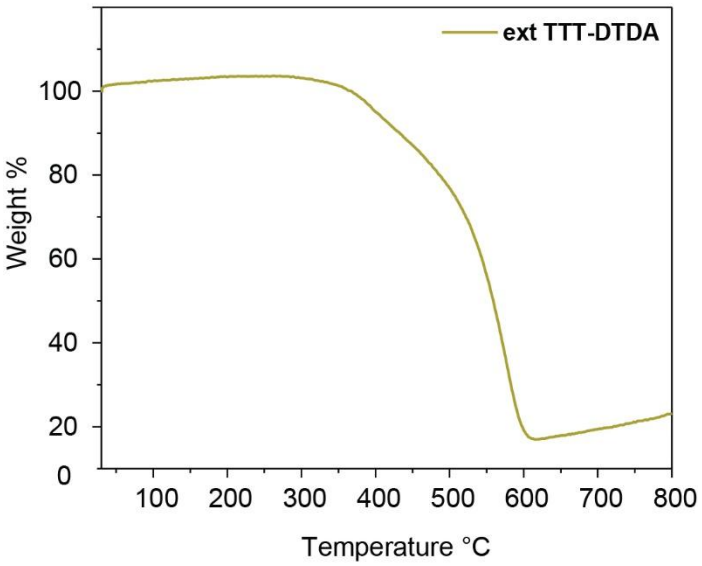

Figure S33. Thermogravimetric analysis (TGA) of extTTT-DTDA COF.

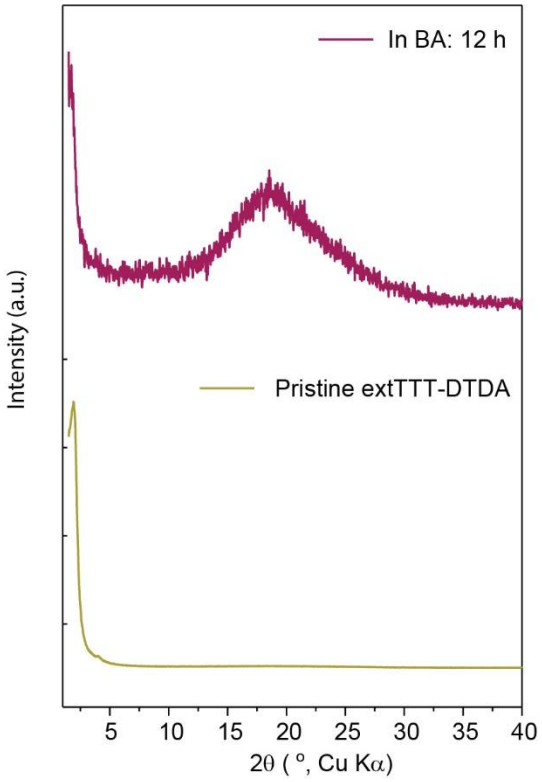

Figure S34. PXRD patterns of extTTT-DTDA in different solvents.

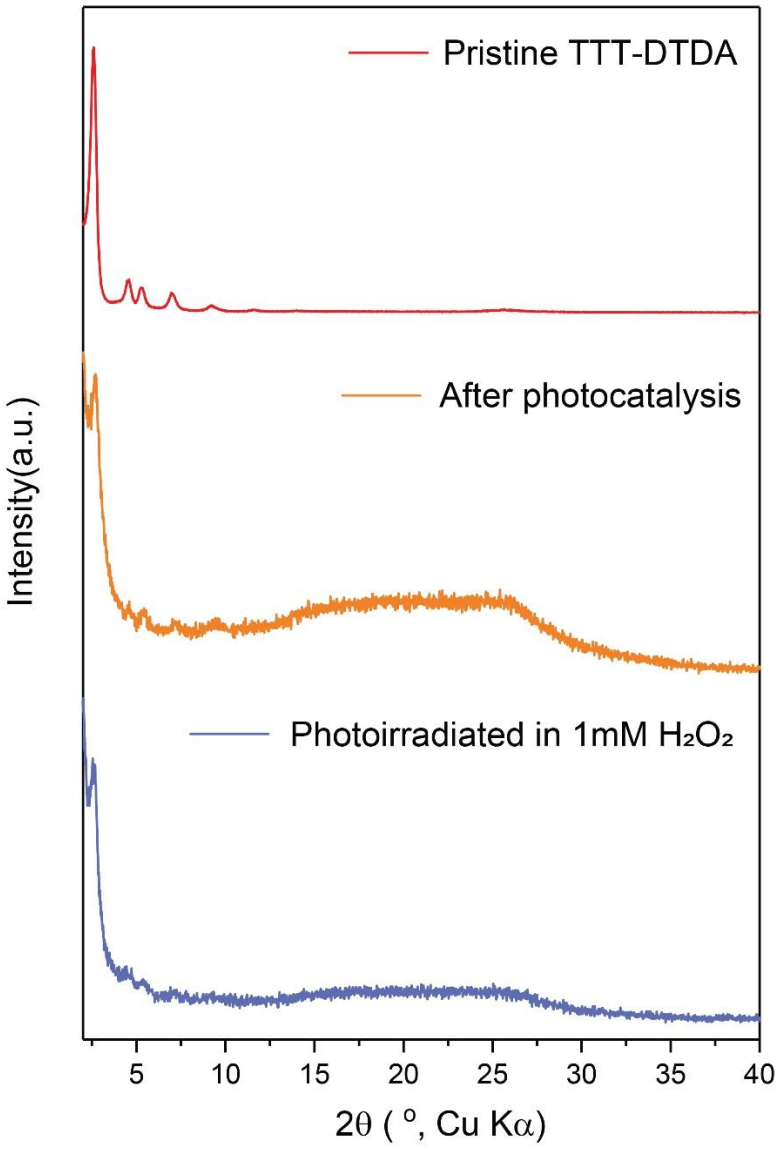

Figure S35. PXRD patterns of pristine TTT-DTDA COF, after photocatalysis, and after photo-irradiation in 1 mM H_2O_2.

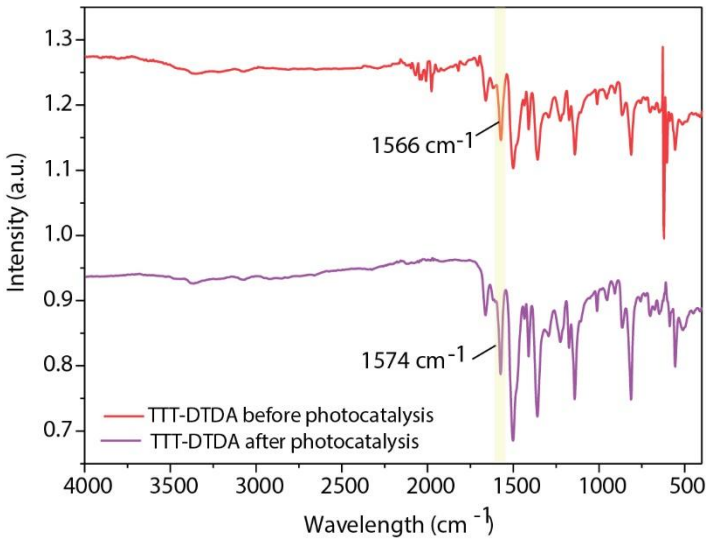

Figure S36. FT-IR spectra before and after photocatalysis for TTT-DTDA COF.

Section S6. Computational studies

2D chemical structures of the TAA-DTDA, TAPB-DTDA, TTT-DTDA, and extTTT-DTDA covalent organic frameworks (COFs) were drawn, and the hexagonal unit cells were defined using GaussView 6, followed by a series of geometry optimization steps. All the geometry optimizations were performed using the density functional theory (DFT) calculation tool as implemented in the Vienna Ab-initio Simulation Package (VASP), following a previously reported protocol.[3] In brief, the atomic potential is described by the standard pseudopotential library of Perdew–Burke–Ernzerhof (PBE) in the projector augmented wave (PAW) method. The cut-off energy for a plane wave was set to 520 eV due to the presence of O atoms. The energy convergence criterion was set to 10^{-6} eV in an iterative solution of the Kohn−Sham equation. The ionic convergence criterion was set to 10^{-5} eV. ~20 Å vacuum was added in the z direction for optimization of the monolayers. Brillouin zone integration was accomplished by a 3 × 3 × 1 Monkhorst−Pack k-point mesh. For bulk, a van der Waals (dispersion) correction was specified by Gimme's D3 method with the Becke-Johnson damping function (DFT-D3(BJ)). Monkhorst-Pack k-point was set to 3 × 3 × 15 for the AA stacked (bulk) geometry optimization. Simulated XRD patterns for the eclipsed (AA) stacked geometries were obtained using VESTA. Band structure, density of states (DOS), and the band-decomposed-electron-densities of frontier orbitals (HOMO/LUMO) were computed on the optimized geometries using standard protocols. The electronic energy profile of the reaction 2 $H_2O + O_2 \rightarrow 2\ H_2O_2$ was studied by optimizing the reactant, product, and various possible intermediates within the pore of TTT-DTDA COF. Two layers of the AA stacked geometry were taken in the unit cell, and Monkhorst-Pack k-point was set to 3 × 3 × 7.

Local potential mapping:

Electrostatic potential maps were computed by enabling LVTOT = .TRUE. in VASP, producing the total local potential including ionic, Hartree, and exchange-correlation contributions as follows:

$$V\_{LOCPOT}(r) = V\_{ionic}(r) + V\_{Hartree}(r) + V\_{XC}(r)$$

where $V_{ionic}(r)$ is the ionic potential as mimicked by the pseudopotentials and $V_{Hartree}(r)$ is the Hartree potential and $V_{XC}(r)$ is the (semi-)local exchange-correlation potential. This potential was subsequently projected onto the charge density isosurface (isovalue = 0.005 e/Å^3) using VESTA,

with a red–white–blue color scale spanning –2 eV (red) to +2 eV (blue). This visualization highlights potential variations across the molecular surface, providing insight into potential electrophilic and nucleophilic reactive centers.

Partial atomic charge calculations:

Atomic charges were calculated using the DDEC6 (Density Derived Electrostatic and Chemical) method with the even-tempered reference ion approach, as implemented in the Chargemol program (version 3.5). The required input charge density files were obtained from VASP calculations by setting LAECHG = TRUE, which generates the AECCAR0 (core electron density), AECCAR2 (valence electron density), and CHGCAR files. The total all-electron charge density was constructed as: AECCAR0 + AECCAR2. The summed charge density and the corresponding POSCAR file were used as input to Chargemol. The DDEC6 method, employing even-tempered reference ions, allows for chemically meaningful charge assignment in bulk periodic systems. All calculations were carried out using default Chargemol settings.

Dihedral angle calculations:

Dihedral angles were defined using the four-atom torsion A–B–C–D, where A, B, C, and D are atom indices in the molecule. The angle represents the torsional rotation around the B–C bond, calculated as the angle between the plane formed by atoms A–B–C and the plane formed by B–C–D. Calculations were performed using VESTA with default geometric conventions, where a positive angle indicates a clockwise rotation from plane A–B–C to B–C–D when viewed along the B–C bond vector. All angles are reported in degrees.

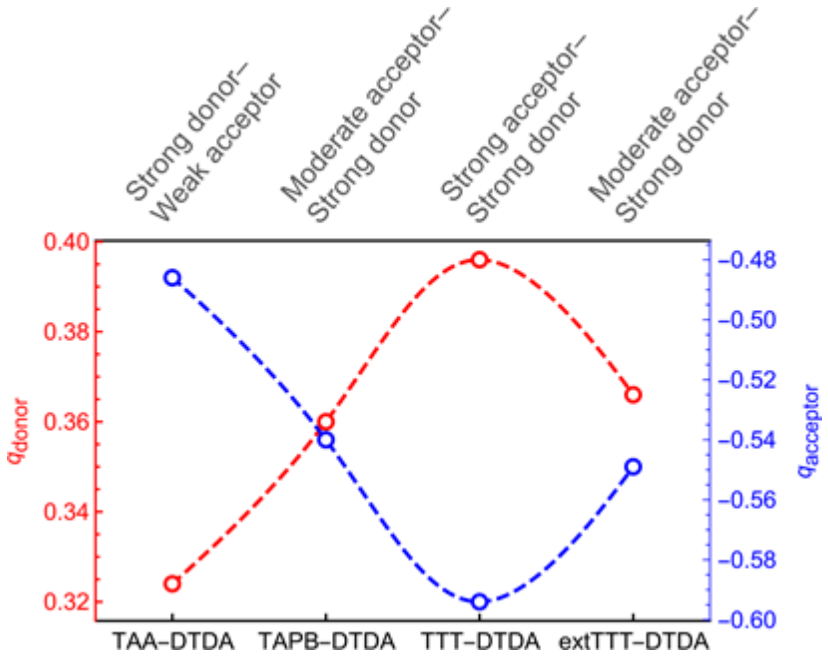

Figure S37. Theoretical estimation of the partial charge distribution for the COFs.

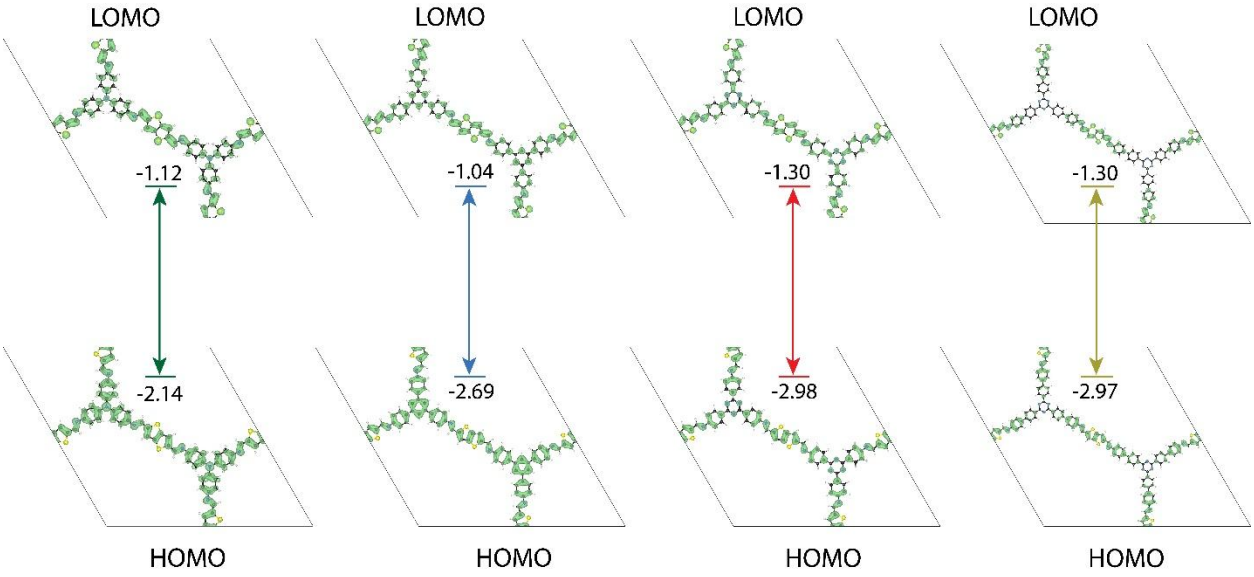

Figure S38. The theoretical distribution of the highest occupied molecular orbital (HOMO) and the lowest unoccupied molecular orbital (LUMO) of TAA-DTDA, TAPB-DTDA, TTT-DTDA, and ext-TTT-DTDA COFs.

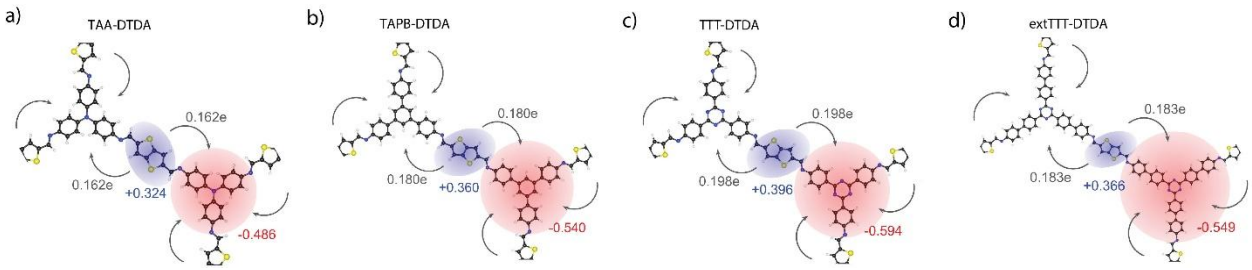

Figure S39. Charge distribution profiles of (a)TAA-DTDA, (b) TAPB-DTDA, (c) TTT-DTDA, and (d) extTTT-DTDA COFs.

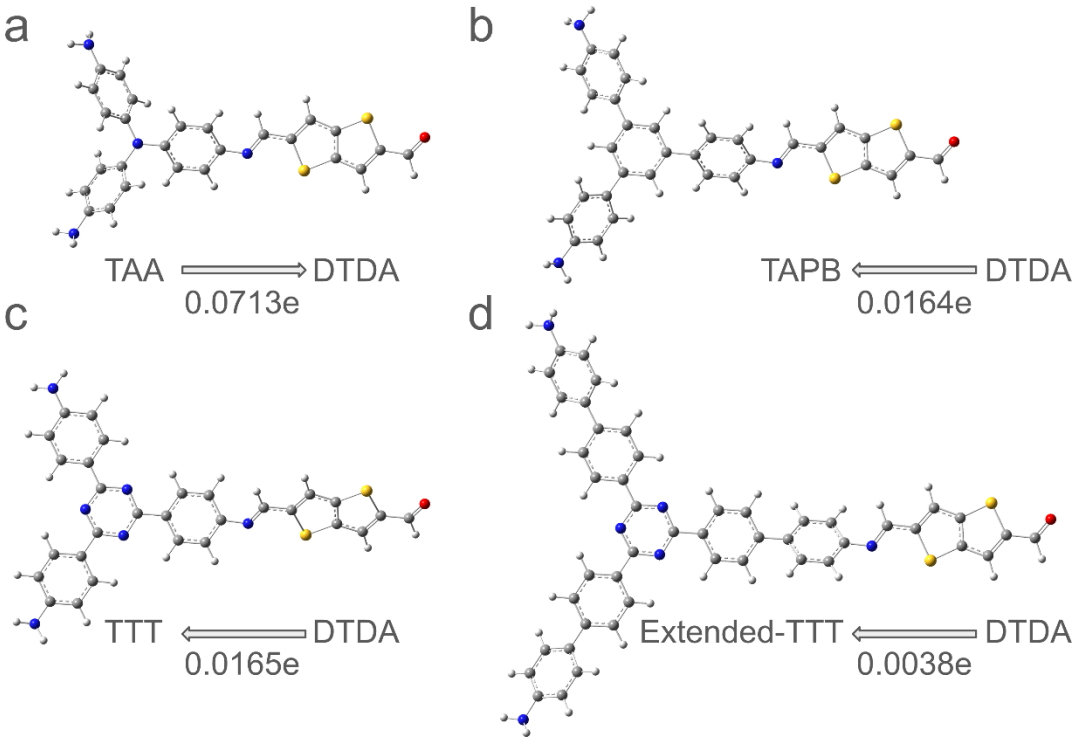

Figure S40. Mulliken charges on (a) TAA-DTDA, (b) TAPB-DTDA, (c) TTT-DTDA, and (d) extTTT-DTDA COFs calculated using non-periodic DFT calculations using fragments.

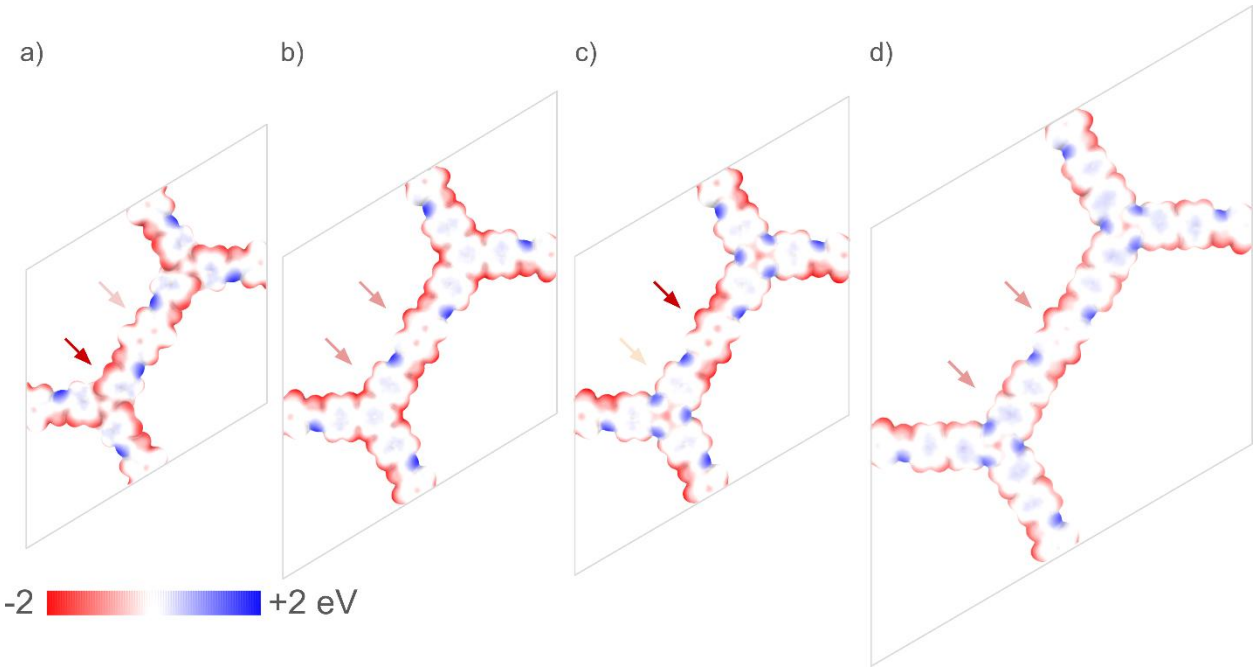

Figure S41. Calculated local potential of (a)TAA-DTDA, (b) TAPB-DTDA, (c) TTT-DTDA, and (d) extTTT-DTDA COFs.

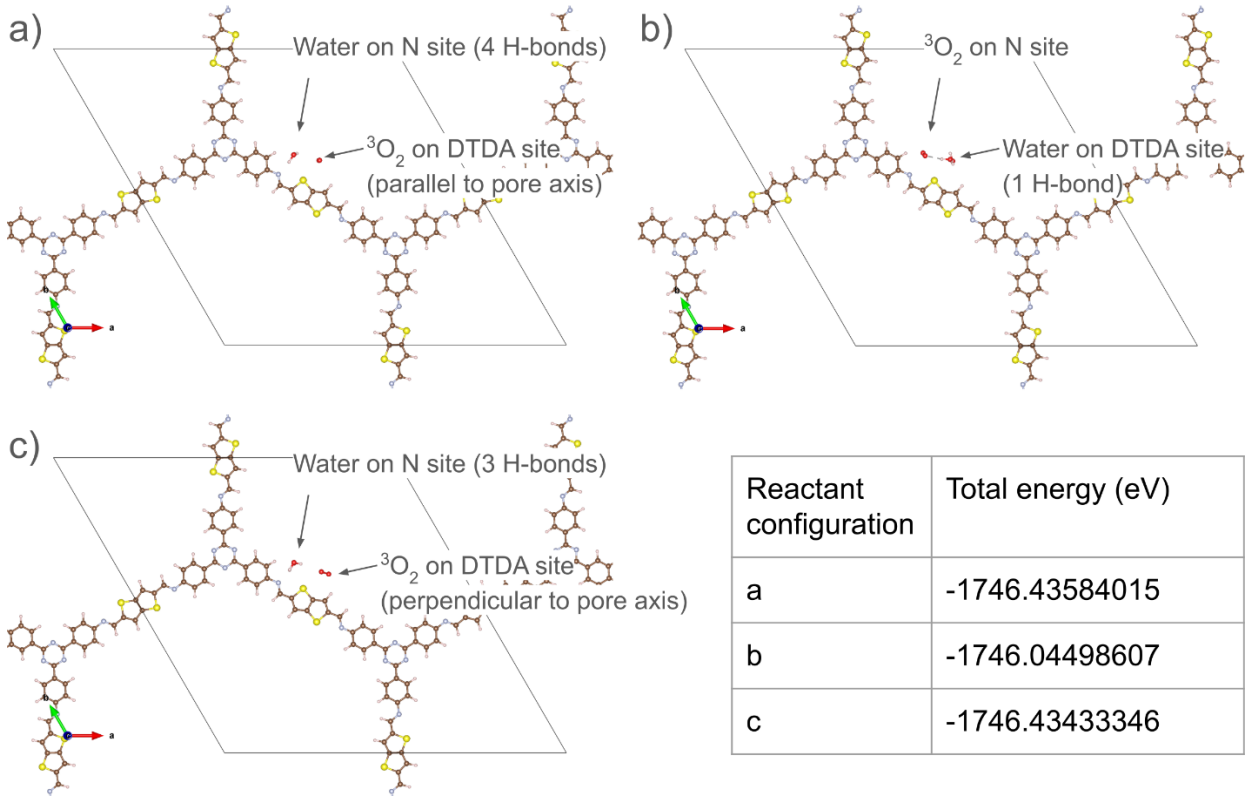

Reactant configuration	Total energy (eV)
a	-1746.43584015
b	-1746.04498607
c	-1746.43433346

Figure S42. Relative energy difference between different binding sites of O_2 on the TTT-DTDA COF.

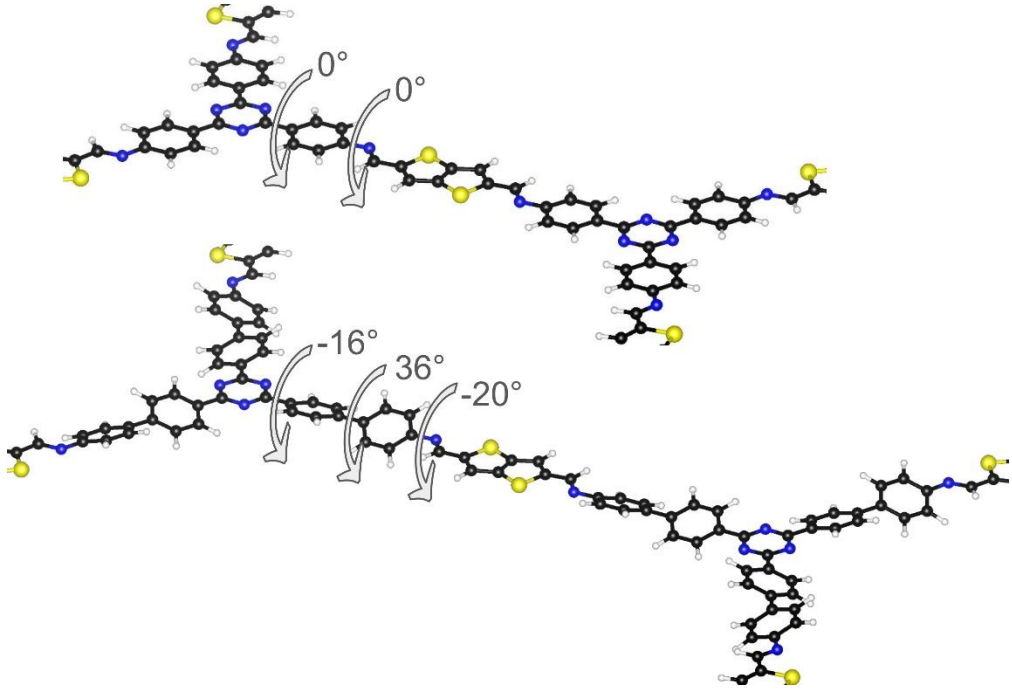

Figure S43. Dihedral angle measurements for (a) TTT-DTDA, and (b) extTTT-DTDA COFs.

Table S5: Performances of some recently reported COF photocatalysts for H_2O_2 generation.

Photocatalysts	**Irradiation conditions (nm)**	**Light Source (W)**	**Reaction medium**	**H_2O_2 generation rate ($\mu mol\ h^{-1}\ g^{-1}$)**	**Irradiation time (min)**	**AQE (%)**	**Ref.**
TAA-DTDA	467	40	Pure water	500	120	5.59	***This work***
TAPB-DTDA	467	40	Pure water	965	120	10.8	***This work***
TTT-DTDA	467	40	Pure water	1265	120	11.1	***This work***
extTTT-DTDA	467	40	Pure water	747	120	8.36	***This work***
TT-DTDA	$\lambda \geq 420$ nm	300	O_2 saturated aqueous solution	1302	120	NA	[3]
TpPy	$\lambda \geq 420$ nm	300	O_2 saturated aqueous solution	1615.5	60	7.7	[4]
HITMS-COF-20	$\lambda \geq 420$ nm	300	O_2 saturated aqueous solution	452	60	2.12	[5]
Por-BQ-COF	$\lambda \geq 420$ nm	300	O_2 saturated alkaline solution (p H = 7-14)	1525	60	5.05	[6]
ThTz-COF	$\lambda \geq 410$ nm	160	O_2 saturated aqueous solution	2506	60	0.16	[7]

DVA COF	420	300	10 mg in water/benzyl alcohol system	84.5	120	2.84	[8]
BDOH-Tb-IM	λ ≥ 420 nm	300	O_2 saturated deionized water	2490	120	NA	[9]
TPT-Cz-phCN	λ ≥ 420 nm	300	Pure water and open air	2534	60	19.1	[10]
PTA0.5@TTB-EB	λ ≥ 420 nm	300	O_2 saturated aqueous solution	897.94 μmol·L−1· h−1	6.6	NA	[11]
TMT-TT COF	420 <λ < 700	300	10 mg photocatalyst in O_2 saturated aqueous solution	1954	180	NA	[12]
TDB-COF	λ ≥ 420 nm	300	O_2 saturated aqueous solution	723.5	240	1.4	[13]
COF-NUST-16	λ ≥ 420 nm	300	H_2O:EtOH = 9:1	1081	120	NA	[14]
Py-Da COF	λ ≥ 420 nm	300	H_2O: BA = 9:1	1242	180	4.5	*[15]*
COF-TAPB-BPDA	λ ≥ 420 nm	300	H_2O: BA = 4:1	1240	120	NA	*[16]*
EBA COF	λ ≥ 420 nm	50	H_2O: EtOH = 9:1	1830	120	4.4	*[17]*
TiCOF-spn	λ ≥ 420 nm	300	H_2O/EtOH = 1 : 9	489.94	300	NA	*[18]*

TpAQ-COF-12	$\lambda \geq 420$ nm	300	Pure water	420	60	7.4	[19]
COF-TfpBpy	> 420	300	Pure water and dry air	700	40	8.1	[20]
Hz-TP-BT-COF	420-600	300	Air saturated pure water	5700	60	17.5	*[21]*
TF_{50}-COF	> 400	300	H_2O: EtOH = 9:1	1739	60	5.1	*[22]*
DETH-COF	> 420	300	Pure water	1012.5	240	0.063 %	*[23]*
CTF-BDDBN	> 420	300	Pure water	70	480	N/A	*[24]*
PMCR-1	420-700	300	O_2 purge and water : ethanol = 10:1	1294	60	14	*[25]*
SonoCOF-F2	Solar Simulator	1440	O_2 saturated pure water	1200	90	4.8	*[26]*
COF-N32	natural sunlight		Ultrapure water	605	720	6.2	*[27]*
TaptBtt	>420	300	O_2 saturated pure water	1407	90	4.6	*[28]*
TZ-COF	> 420	300	Pure water	300	90	0.6	[29]

Section S7. References

[1] Z. Zhang, Y. Hou, S. Zhu, L. Yang, Y. Wang, H. Yue, H. Xia, G. Wu, S.-w. Yang, X. Liu, *Angew Chem Int Ed* **2025**, n/a, e202505286.

[2] J. Zhang, Y. Cao, W. Liu, T. Cao, J. Qian, J. Wang, X. Yao, A. Iqbal, W. Qin, *ChemSusChem* **2022**, 15, e202101510.

[3] Y. Wang, H. Zhao, P. Li, J. Zhang, X. Sun, R. Zhang, Y. Guo, Y. Dong, Y. Zhu, *Chem. Eng. J.* **2024**, *491*, 151825.

[4] Q. Liao, Z. Li, Q. Sun, H. Xu, Y. Wang, Y. Xu, H. Wu, Z. Zhang, Y. Xie, H. Li, D. Wang, G. Li, K. Xi, *ACS Appl. Nano Mater.* **2025**, *8*, 8095.

[5] L. Wang, C. Han, S. Gao, J.-X. Jiang, Y. Zhang, *ACS Catal.* **2025**, *15*, 5683.

[6] H. Li, Y. Li, X. Lv, C. Liu, N. Zhang, J. Zang, P. Yue, Y. Gao, C. Liu, Y. Li, *Adv. Mater.* **2025**, *37*, 2415126.

[7] R.-C. Chen, C.-M. Wu, L.-H. Chung, J. Hu, M.-C. Tang, Z. Lin, X. Yang, Z. Xu, J. He, *Chem. Mater.* **2024**, *36*, 9928.

[8] H. Yu, F. Zhang, Q. Chen, P.-K. Zhou, W. Xing, S. Wang, G. Zhang, Y. Jiang, X. Chen, *Angew Chem Int Ed* **2024**, *63*, e202402297.

[9] X. Peng, Y. Tian, T. Yang, X. Wang, C. Song, A. Kong, *ACS Appl. Mater. Interfaces* **2024**, *16*, 40180.

[10] H. Yan, Y. Peng, Y. Huang, M. Shen, X. Wei, W. Zou, Q. Tong, N. Zhou, J. Xu, Y. Zhang, Y.-X. Ye, G. Ouyang, *Adv. Mater.* **2024**, *36*, 2311535.

[11] Q. Rong, X. Chen, S. Li, S. He, *ACS Appl. Mater. Interfaces* **2024**, *16*, 5758.

[12] M. Deng, L. Wang, Z. Wen, J. Chakraborty, J. Sun, G. Wang, P. Van Der Voort, *Green Chem.* **2024**, *26*, 3239.

[13] Z. Zhou, M. Sun, Y. Zhu, P. Li, Y. Zhang, M. Wang, Y. Shen, *Appl. Catal. B Environ.* **2023**, *334*, 122862.

[14] M. Wu, Z. Shan, J. Wang, T. Liu, G. Zhang, *Chem. Eng. J.* **2023**, *454*, 140121.

[15] J. Sun, H. Sekhar Jena, C. Krishnaraj, K. Singh Rawat, S. Abednatanzi, J. Chakraborty, A. Laemont, W. Liu, H. Chen, Y.-Y. Liu, K. Leus, H. Vrielinck, V. Van Speybroeck, P. Van Der Voort, *Angew Chem Int Ed* **2023**, *62*, e202216719.

[16] T. Yang, Y. Chen, Y. Wang, X. Peng, A. Kong, *ACS Appl. Mater. Interfaces* **2023**, *15*, 8066.

[17] L. Zhai, Z. Xie, C.-X. Cui, X. Yang, Q. Xu, X. Ke, M. Liu, L.-B. Qu, X. Chen, L. Mi, *Chem. Mater.* **2022**, *34*, 5232.

[18] W.-K. Han, H.-S. Lu, J.-X. Fu, X. Liu, X. Zhu, X. Yan, J. Zhang, Y. Jiang, H. Dong, Z.-G. Gu, *Chem. Eng. J.* **2022**, *449*, 137802.

[19] X. Zhang, J. Zhang, J. Miao, X. Wen, C. Chen, B. Zhou, M. Long, *Chem. Eng. J.* **2023**, *466*, 143085.

[20] M. Kou, Y. Wang, Y. Xu, L. Ye, Y. Huang, B. Jia, H. Li, J. Ren, Y. Deng, J. Chen, Y. Zhou, K. Lei, L. Wang, W. Liu, H. Huang, T. Ma, *Angew Chem Int Ed* **2022**, *61*, e202200413.

[21] R. Liu, Y. Chen, H. Yu, M. Položij, Y. Guo, T. C. Sum, T. Heine, D. Jiang, *Nat. Catal.* **2024**, *7*, 195.

[22] H. Wang, C. Yang, F. Chen, G. Zheng, Q. Han, *Angew Chem Int Ed* **2022**, *61*, e202202328.

[23] G. Pan, X. Hou, Z. Liu, C. Yang, J. Long, G. Huang, J. Bi, Y. Yu, L. Li, *ACS Catal.* **2022**, *12*, 14911.

[24] L. Chen, L. Wang, Y. Wan, Y. Zhang, Z. Qi, X. Wu, H. Xu, *Adv. Mater.* **2020**, *32*, 1904433.

[25] P. Das, J. Roeser, A. Thomas, *Angew. Chem. Int. Ed.* **2023**, *62*, e202304349.

[26] W. Zhao, P. Yan, B. Li, M. Bahri, L. Liu, X. Zhou, R. Clowes, N. D. Browning, Y. Wu, J. W. Ward, A. I. Cooper, *J. Am. Chem. Soc.* **2022**, *144*, 9902.

[27] F. Liu, P. Zhou, Y. Hou, H. Tan, Y. Liang, J. Liang, Q. Zhang, S. Guo, M. Tong, J. Ni, *Nat. Commun.* **2023**, *14*, 4344.

[28] C. Qin, X. Wu, L. Tang, X. Chen, M. Li, Y. Mou, B. Su, S. Wang, C. Feng, J. Liu, X. Yuan, Y. Zhao, H. Wang, *Nat. Commun.* **2023**, *14*, 5238.

[29] Y. Mou, X. Wu, C. Qin, J. Chen, Y. Zhao, L. Jiang, C. Zhang, X. Yuan, E. Huixiang Ang, H. Wang, *Angew Chem Int Ed* **2023**, *62*, e202309480.